DIPLOMARBEIT

Practical Evaluation of the Leica Geosystems AP20 AutoPole

zur Erlangung des akademischen Grades

Diplom-Ingenieur

im Rahmen des Studiums

Geodäsie und Geoinformation

eingereicht von

Manuel Zechner BSc.

Matrikelnummer: 01427372

ausgeführt im Forschungbereich Ingenieurgeodäsie (E120.5)
am Department für Geodäsie und Geoinformation
der Fakultät für Mathematik und Geoinformation der Technischen Universität Wien

Betreuung:
Univ. Prof. Dr.-Ing. Hans-Berndt Neuner (Technische Universität Wien)

Wien, im September 2024

(Manuel Zechner) (Hans-Berndt Neuner)

Affidavit

I declare in lieu of oath, that I wrote this thesis myself in accordance with the recognised principles for scientific papers. All resources used, especially the literature, are listed in this thesis. If text passages from sources are used literally, they are marked as such.

I confirm that this work is original and has not been submitted elsewhere for any examination, nor is it currently under consideration for a thesis elsewhere.

Wien, im September 2024

Manuel Zechner

Danksagung

Beginnend möchte ich mich bei Herrn Univ. Prof. Dr.-Ing. *Hans-Berndt Neuner* für die Möglichkeit der Durchführung sowie die Unterstützung und Betreuung bedanken. Das ehrliche und inhaltliche Feedback wusste ich zu jedem Zeitpunkt sehr zu schätzen und es war sehr wertvoll im Zuge der Ausarbeitung dieser Arbeit.
Ein weiterer Dank gilt Herrn Dipl. Ing. *Tomas Thalmann* für sämtliche Hilfestellungen und Inputs, sowohl während der Bachelorarbeit, als auch während der Bearbeitung dieser Diplomarbeit.
Bedanken möchte ich mich ebenso bei Herrn Dipl. Ing. *Hannes Maar* für die Informationen, Ideen sowie die Unterstützung, die mir stets hilfreich waren.
Weiters bedanke ich mich bei Herrn *Leonhard Köpf* für das mir entgegengebrachte Vertrauen.
Besonders möchte ich mich bei *meiner Familie* bedanken. Dass es mir ermöglicht wurde, dieses Studium auszuführen, war für mich zu keinem Zeitpunkt selbstverständlich und ich wusste dies stets zu schätzen. Danke, dass ihr mich auf diesem Weg unterstützt habt und mir somit die Möglichkeit gegeben habt, einen wichtigen Grundstein für mein weiteres Leben zu legen.
Un agradecimiento especial a mi pareja *Carolina*. Gracias por tu apoyo constante y tu respaldo, porque sin tu ayuda esta tesis de maestría no habría sido posible. Agradezco mucho que siempre me hayas motivado y me hayas acercado al final del túnel una y otra vez. Tu apoyo ha tenido un gran impacto en la finalización de mis estudios.
Last but not least möchte ich mich bei meinen *Studienkollegen* bedanken. Die Zeit des Studiums brachte viele unvergessliche Erlebnisse aber auch Freundschaften, die das Studium überdauerten und für die ich sehr dankbar bin.
Dieser Dank gilt auch *meinen Freunden* in meiner Heimat, welche mich trotz der Distanz immer so empfingen, als wäre ich nie weg gewesen.

Abstract

The expansion of classical surveying instruments into multi-sensor systems has enlarged both the application area of instruments and their users in recent years. Innovative technologies are making their way into surveying, leading to increased efficiency of equipment and potentially higher accuracy of measurement data on the technical side. Multi-sensor systems are state-of-the-art in modern surveying.

However, the accompanying technical complexity of these systems often raises questions for users about the achievable accuracy in everyday use and also about the limits of such systems.

The *AP20 AutoPole*, presented by *Leica Geosystems* in 2022, is an example of the extension of classical surveying solutions with innovative technology. The tilt-compensated measurement of coordinates expands the application range and facilitates workflow at the same time.

In the course of this master thesis, this system was to be evaluated. Initially, a theoretical description of the entire system and methodology is provided. During the investigations, a general comparison of the AP20 AutoPole to conventional geodetic methods for point measurement is given. Subsequently, the inertial measurement unit's (IMU) initialization is examined in detail, and the influence of different types of motion is analyzed. Based on the results, the insights gained are finally examined and evaluated in a stakeout scenario using tilt-compensation.

Kurzfassung

Die Erweiterung der klassischen Vermessungsinstrumente hin zu Multisensorsystemen hat in den vergangenen Jahren sowohl das Anwendungsgebiet von Instrumenten als auch deren Nutzern erweitert. Innovative Technologien halten auch in der Vermessung Einzug und führen somit zur Steigerung der Effizienz von Equipment, aber auch zur Steigerung der möglichen Genauigkeit der Messdaten auf technischer Seite. Multisensorsysteme sind „state of the art“ in der modernen Vermessung.

Die miteinhergehende technische Komplexität dieser Systeme stellt jedoch die Nutzer oft vor die Fragestellung der erreichbaren Genauigkeit in der alltäglichen Anwendung und ebenso, wo die Grenzen solcher Systeme liegen.

Der von *Leica Geosystems* im Jahr 2022 präsentierte *AP20 AutoPole* ist ein Beispiel für die Erweiterung klassischer Vermessungslösungen um innovative Technologie. Die neigungskompensierte Messung von Koordinaten erweitert hierbei den Anwendungsbereich und erleichtert zugleich den Arbeitsablauf.

Im Zuge dieser Master-Thesis sollte dieses System evaluiert werden. Zu Beginn wird eine theoretische Beschreibung des Gesamtsystems und der Methodik gegeben. Im Zuge der Untersuchungen erfolgt eine allgemeine Einordnung des AP20 AutoPole zu herkömmlichen geodätischen Methoden zur Punktmessung. Vertiefend wird darauffolgend die Initialisierung der inertialen Messeinheit (IMU) betrachtet und der Einfluss von unterschiedlichen Bewegungsformen analysiert. Aufbauend auf den Resultaten werden die gewonnenen Erkenntnisse schliesslich in einem Absteckungsszenario mit Neigungskompensation betrachtet und evaluiert.

Contents

1. Introduction

Looking at the period from the beginnings of surveying until today, it becomes evident that the fundamental task has not changed: the determination of the position of points in a two- or three-dimensional space and the description of these point positions based on coordinates with respect to a reference frame. Similarly, the observed quantities have not changed since then. The required information is represented in the form of distances and angles.

However, over the time, especially the technology and methodology for determining the mentioned observed quantities have changed. Observing the progress over the aforementioned period until today, it can be seen that innovation leads to gains in accuracy, efficiency, and a reduction in possible errors caused by user interaction.

Comparing the development of surveying instruments to other technical products, the innovation of measuring instruments may seem slow. However, considering the long lifecycle of an instrument and its requirement for accuracy, a long development time is justified. Also, the high purchase price leads users to keep the products in use for as long as possible to spread the costs over many years.

This long lifecycle does not prevent innovative new technologies from being introduced in the surveying industry. For example, in recent years, the race for market dominance has not been led by increasingly accurate instruments. The focus has shifted more towards features or enhancements to the equipment. For instance, laser scanning has been integrated into total stations, such as the *Leica Geosystems Multistation Nova MS60*. Laser scanning on total stations is a limited variant compared to stand-alone laser scanners, with the advantages of a total station (e.g., stationing in a control point field). Similarly, prisms have been developed to allow for improved prism tracking and targeting (e.g., *Trimble MT-1000 Target* or *Trimble AT360 Target*). These active prisms are based on an optical method where an LED signature is actively emitted to be detected by the total station.

In recent years, a trend has emerged where inertial sensors have been increasingly integrated into various instruments. While inertial systems have been widely used for decades in navigation tasks, their application in surveying is a relatively new technology. Initially, they were primarily integrated into Global Navigation Satellite System (GNSS) sensors, such as the GNSS Receiver *Trimble R10*. At the outset, tilt-compensated measurements were associated with high effort. This was due to the use of electronic compasses, which required on-site magnetometer measurements to determine the magnetic north direction. Additionally, extensive calibrations had to be performed in the field. This high temporal and resource-intensive effort thus reduced the benefits, and the adoption of this technology remained limited. It was only through the introduction of Micro-Electro-Mechanical

Systems (MEMS) Inertial Measurement Units (IMU) that these weaknesses could be addressed, leading to benefits for the user. A milestone in this regard was the introduction of the *Leica Geosystems GS18T RTK GNSS Rover*. *Luo et al.* (2018) describe the advantages of applying MEMS IMUs and the increase in efficiency without compromising accuracy.
Ultimately, MEMS IMU technology is state-of-the-art in modern GNSS receivers. This also raised the question of how inertial sensors could be applicable in terrestrial geodetic measurements and how users can benefit from them. *Thalmann et al.* (2020) propose an approach where MEMS IMUs are used for tilt compensation of a pole, which also provides a promising level of accuracy. The study was conducted using a consumer-grade MEMS IMU, and the compensation model is based on Euler angles. As will be shown later in this work, these angles lead to a singularity problem.
Leica Geosystems pursued a similar approach independently and brought the *AP20 Autopole* to the market as a product. The difference from *Thalmann et al.* (2020) lies mainly in the real-time application of the system and the extension of the system with additional features such as automatic height measurement at the pole and an optical solution for prism search. *Maar* (2022) describes the fundamentals and application of the AP20 AutoPole as well as the issues attempted to be addressed with this product.
This includes a general description of the necessity of sensor initialization and recommended initialization movements. However, the question remains which initialization movements have a particularly positive impact and which have a minimal effect.

As part of this work, the focus will be on this sensor initialization, and different types and executions of movements will be analyzed. After a general case study on the application of the AP20 AutoPole in geodetic tasks, the initialization methods will be evaluated. Subsequently, these findings will be applied to a practical surveying application, stakeout, and the impact of initialization will be discussed.
At the end of this thesis, the following questions should be answered:

1. How does the performance of the AP20 AutoPole compare with conventional point acquisition methods, and what advantages and disadvantages can be derived from this?

2. Do different initialization movements influence the quality of attitude determination, and can specific movement forms be recommended?

3. Is there a "good" and "bad" form of initialization, and how do these affect stakeout accordingly?

Based on the results, this work aims to provide a "best practice" recommendation for initialization, which will be discussed conclusively. Additionally, an outlook on possible future applications will be provided.

2. Fundamentals

For a better understanding of the later described investigation, this section provides a theoretical base of the components that are necessary for tilt compensated measurements with regard to the solution brought to the market by *Leica Geosystems*. In the following text, the abbreviation "Leica" is used, which exclusively refers to Leica Geosystems AG. The overall system consists of a motorized total station and the pole where the AP20 AutoPole is mounted. Even though a total station has a wide range of applications and functionalities, the focus in section 2.1 is on the functionalities needed for tilted pole measurements.
In subsection 2.2, a general foundation about Inertial Navigation Systems (INS) is provided. This includes a general view on strapdown INS in 2.2.2, a closer look at the different coordinate systems in this context in 2.2.1 as well as the characteristics of IMUs in 2.2.3.

2.1. Total Station: Leica Nova Multistation MS60

Despite numerous advancements since the beginning of surveying and the start of the development of surveying instruments, the underlying working principle has remained consistent. It involves measuring distances and angles to determine coordinates. While these measurements were originally separate processes in the early days of surveying, technological progress combined them into a single measuring instrument: the tachymeter. Regardless of design and manufacturer, tachymeters are described by the following axis definition:

- **Aiming Axis**: defined by the objective and the crosshairs
- **Tilting Axis**: Telescope's axis of rotation
- **Vertical Axis**: defined by the orientation of the local gravity vector

By this, the following requirements have to be necessarily fulfilled by manufacturing:

- the zero point of distance measurement coincides with the intersection point of the three axes
- the horizontal circle of the angle measuring unit has to be orthogonal to the standing axis
- the vertical circle of the angle measuring unit has to be parallel to the standing axis
- the aiming axis has to be orthogonal to tilting axis
- the tilting axis has to be orthogonal to aiming axis

With the expansion of applicability, such as through newer features like scanning or imaging, these total stations have become versatile measuring instruments. They are widely used today and can be found in total stations from various manufacturers, such as Trimble, Topcon, or Leica, to name just a few here. But still the main task is to determine point locations with coordinates or bring them from the plan back to real world.

In the further course of this chapter, a total station called *Multistation Nova MS60* from Leica will be discussed. This device was used during investigations.

General

Leica's *Multistation MS60* (see fig. 2.1) combines the functionality of a classical total station with additional functions. For example, it is possible to perform scanning tasks with this instrument. This further expands the portfolio and range of applications. In the further text, *Multistation MS60* will be called MS60 to increase the readability of the text.

In the following, the components are briefly described. The focus is on components and their functions, which are also relevant when using the AP20 AutoPole.

Kleemaier (2018: p. 25-36) classifies the structure of a totalstation in three main parts:

- **Telescope**: Distance measurement unit, automatic aiming (ATR)
- **Alidade/sensor board**: Angular reading (horizontal, vertical), tilt measurement
- **Application board**: operating system, data processing

In general, the mentioned parts are non-separable. The main focus on the following chapter is on the telescope and the alidade.

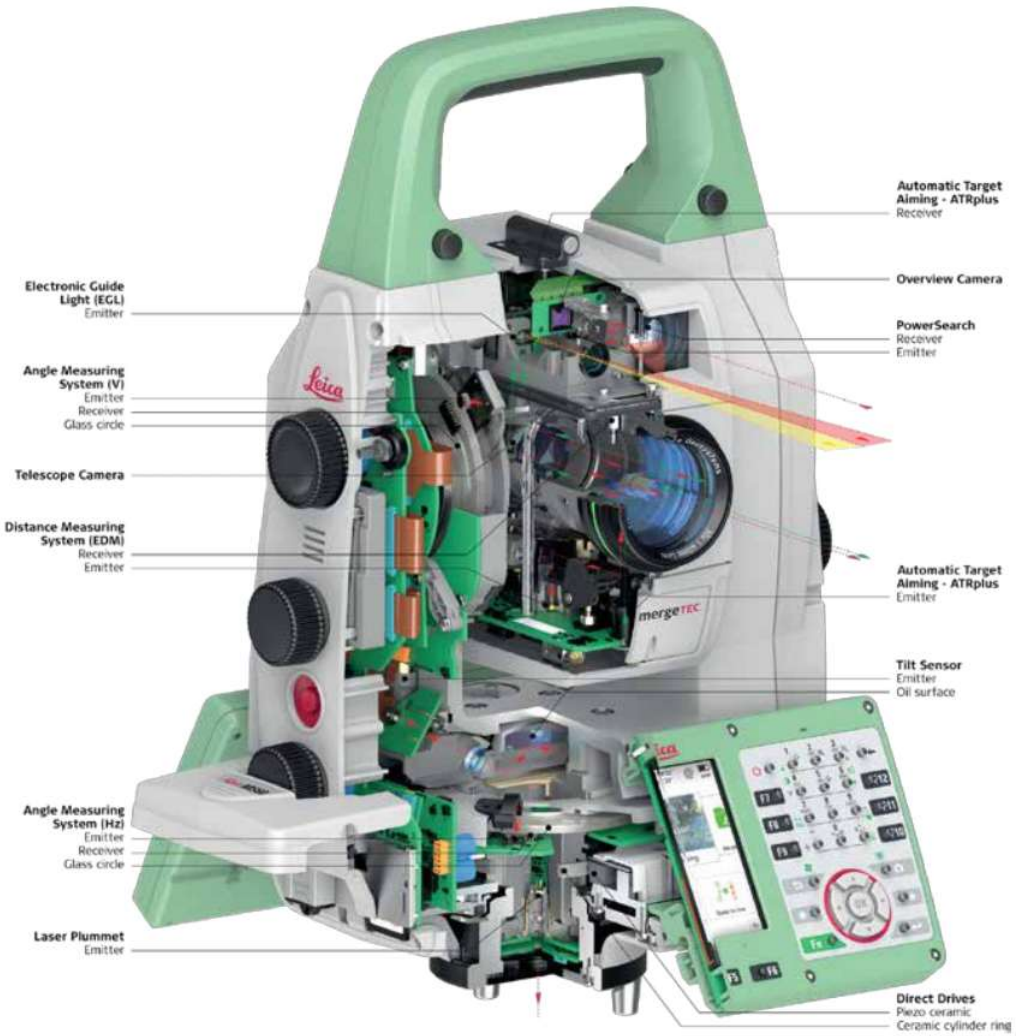

Figure 2.1: Cutaway-drawing of Multistation MS60 (*Maar*, *Zogg* (2017), p.4)

For the sake of completeness, the field software used on the latest Leica total station is *Leica Captivate*, which also performs the onboard data processing. Also during the investigations shown later in this thesis, *Leica Captivate* was used.

Alidade

The alidade is the U-shaped base that enables rotation in the horizontal plane and serves a a support for the telescope. To measure this rotation, it is essential to have an unchanged reference. This is facilitated by the tribrach, which is either fixed to the ground with the tripod or, for example, with a pillar.
Subsequently, the alidade also serves as the platform for a large part of the sensors and additional components.

After leveling using the adjusting screws of the tribrach, any residual inclination is corrected by a 2-axis tilt compensator. This device comprises a light diode directing light through a prism with a printed barcode. *Zogg* et al. (2009, p. 7 ff) refers in the publication to a Leica TS30, which was launched earlier than MS60. But the basic functional principle is in use in MS60 as well and makes this part of the publication still valid for MS60.
The light beam undergoes two reflections within the prism before passing through a lens onto a line sensor, which detects the barcode as a bright-dark variation. The arrangement of the barcode lines allows simultaneous indication of longitudinal and transverse deviations. Deviations from the desired values or displacements along the axes determine the deviation from the horizontal, which is then used to correct angular measurements. The principle is shown in fig. 2.2.

Zogg et al. (2009: p. 8-10) describes the functional principle of the motorization in the MS60, which is achieved through a piezo drive mechanism. The piezo effect, a phenomenon in physics, involves generating electrical voltage by deforming crystalline minerals, either naturally or artificially. In the case of the MS60, the reverse piezo effect is utilized to facilitate horizontal and vertical rotations of the total station. This involves converting the expansion or contraction of minerals into rotational movement. The mechanism comprises opposing piezoelectric ceramic units divided into electrodes, which, when activated by alternating current, determine the direction of rotation. The kinetic energy is then transferred to a ceramic ring fixed to the axis, enabling rotation (see fig. 2.3). This drive offers advantages such as high acceleration, speed, and wear-free operation, with particular emphasis on precision due to its small step width.

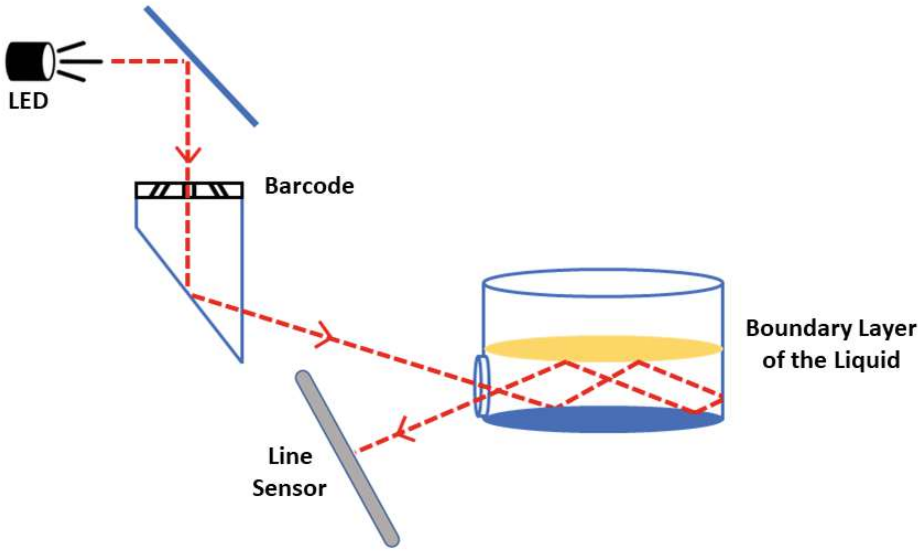

Figure 2.2: Principal of the 2-axis tilt compensator (based on *Zogg et al.* (2009, p.7)

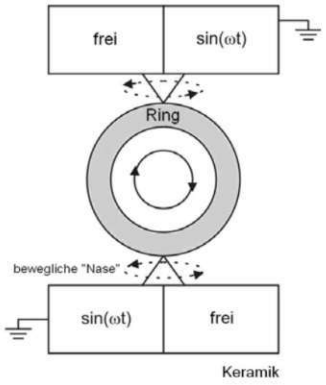

Figure 2.3: Principal of the piezo drives (see *Zogg* et al. 2009, p.9)

Zogg et al. (2009, p.6) describes the functional principle of the angle measurement units. In this publication, the authors refer again to the total station TS30 by Leica. The basic functional principle is unchanged to today's MS60 and can be used here to describe the workflow of the angular measurement units.

The horizontal angle recording unit (shown in fig. 2.4), situated in the alidade's base, employs an optical method for angular measurement. It comprises angle measuring units positioned around the axis of rotation, both horizontally and vertically. These units feature a glass circle with integrated coding, characterized by a pseudo-random pattern of black lines and varying spaces between them. The evaluation unit is aware of this code pattern. A light beam, emitted from a diode and directed via prisms onto a line sensor, passes through the coded circle, resulting in a light-dark change detected by the sensor. A minimum of 10 graduation marks is required for initial angle determination, while a mini-

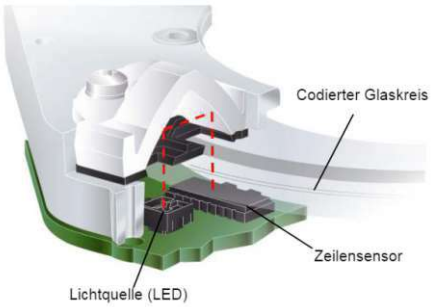

Figure 2.4: Principal of the horizontal Angle Measurement, described by a Leica TS30, which works after the same functional principle (see *Zogg* et al. 2009, p.6)

mum of 30 code strokes improves interpolation accuracy. An internal algorithm processes this data to determine the measured variable. The presence of four angle encoders offers the advantage of eliminating π-periodic phase errors. With just two encoders, the error caused by the eccentricity of the standing axis can be compensated for. Moreover, the encoders contribute to controlling the angle measuring system. The enhanced accuracy and reliability facilitated by the four encoder units allow for precise positioning during automated control by the drives, eliminating the need for iterative corrections to achieve a defined position. The vertical drive operates on a similar principle and is mounted at the turning axis of the telescope.

Telescope

The telescope is the vertically movable part that is pivoted in the middle of the alidade's branches. This element primarily contains the sensors for target search and tracking as well as the distance measurement unit and two cameras.

The telescope integrates cameras positioned strategically to aid users in targeting, especially for challenging sights like those near the zenith. These cameras offer real-time video streams displayed on the total station's display unit. Additionally, they facilitate photography and panoramic imaging for documentation and photogrammetric measurements. The overview camera, situated eccentrically above the optical path, features a 5 MP CMOS camera. The on-axis camera, is integrated into the optical path via a mirror system with the same resolution but a possible higher zoom level.

Adjacent to the overview camera is the PowerSearch Unit, which facilitates prism searching, particularly useful when the line of sight is lost or when locking onto a prism before surveying. It operates through a sensor unit with an associated algorithm, executing a horizontal rotary movement around the instrument's standing axis. During rotation, a laser diode creates a fence with a specific opening angle. If a prism is detected within this rotation, the laser beam reflects off it and is captued by the receiver unit. An algorithm

determines if the reflection is from a reflector or another reflective surface and activates a vertical search if necessary. During this, the telescope moves vertically and enables the Automatic Target Recognition (ATR) unit.
The ATR function comprises transmitter and receiver units. A laser beam is emitted and is guided through the telescope's beam path via mirrors. Dynamic energy control adjusts the laser's brigthness for optimal detection. This means, that the energy of the emitted laser beam is constantly adjusted due to influences such as meteorological conditions and the unknown distance between the total station and the reflector. Reflected beams are conducted through a bandpass filter and afterwards analyzed by algorithms to distinguish between prisms and non-prisms, like reflective vests. Different energy adjustments create gray images for analysis. A spot center determination on the CMOS sensor enables the calculation of horizontal and vertical offset angles to the target point center.

The MS60 utilizes a hybrid approach combining time-of-flight and phase comparison methods to determine distances. The time-of-flight technique involves measuring the runtime of a laser pulse. However, its precision is limited by the inherent inaccuracies of commercial timekeeping devices. Conversely, the phase comparison method calculates distances based on phase shifts in modulated signals by iteratively reducing the wavelength and increasing the frequency.
Bayoud (2006) describes, how Leica's MS60 integrates these methods through a so-called system analyzer, enabling various measurement modes and high-frequency operation, thereby enhancing both accuracy and selectivity.

Radio Handle

In addition to internal Bluetooth communication within the total station, which facilitates remote control via controllers over short distances, a radio handle extension is required for data exchange between the total station and AP20 AutoPole. The RH18 radio handle, designed specifically for the AP20 AutoPole with tilt compensation, includes two antennas for Bluetooth Low Energy (BLE) and Bluetooth Classic.
Described in *Bluetooth SIG* (2024, p.7), Bluetooth technology enables wireless communication between devices without the need for a network or additional equipment beyond a Bluetooth module in each device. BLE, introduced with version 4.0, allows for point-to-point communication as well as networking among multiple BLE modules with reduced energy consumption as a primary focus.
BLE uses the license-free 2.4 GHz band. This extends over 80 channels in the range between 2.402 GHz and 2.48 GHz. The frequency range also includes many other applications such as Wi-Fi Internet, which can limit the range of Bluetooth in urban areas.

2.2. Theory of Inertial Navigation Systems

Inertial sensors offer versatile applications. Originally applied in inertial navigation, such sensors are now utilized in various fields, including vehicles and metrological tasks. Generally, an inertial measurement unit (IMU) typically describes a combination of an accelerometer and a gyroscope. Depending on the application, these sensors may also be integrated individually.
The following chapter begins with an overview of the underlying coordinate systems as well as a basic description of strapdown inertial navigation systems. Subsequently, the focus shifts to the evaluation of sensor data leading to usable measurements, specifically addressing inertial measurement units. Finally, a closer examination of their application in attitude determination is presented.

2.2.1. Coordinate Frames

To describe motion, orientation, or position, it is obvious that a defined reference frame is necessary. This can be fundamentally arbitrarily defined, but a thoughtful definition facilitates application mathematically, physically and also technically.
In the literature, there is often a description of a right- or left-handed coodinate system (i.e. see Groves (2013), p.24). In the further description of this chapter, reference is made to right-handed coordinate systems. This is given when the shortest rotation of the x-axis to the y-axis (in the plane) occurs in the mathematically positive direction (counterclockwise), and as the name suggests, it can be visualized by the right hand.
The degree of freedom of a three-dimensional coordinate systems results in 6DOF.
Generally, depending on usage, sensors are typically positioned so that their orientation aligns with the direction of interest. For example, in an aircraft, the axes are defined to point in the possible directions of movement. Figure 2.5 illustrates this principle. This figure also shows the corresponding measured values along the axes, where a represents acceleration, m represents magnetometer data, and ω represents rotation about the axis.

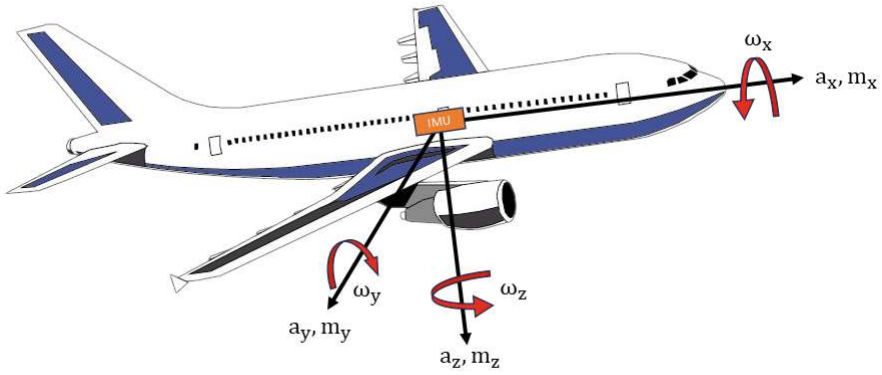

Figure 2.5: IMU coordinate system with corresponding measured values along axes (adapted from Groves (2013), p. 29)

However, the theory described so far are based on an internal sensor coordinate system. This definition is important regarding the individual measured values, but it is meaningless for statements without an external coordinate frame in which the sensor moves. Such a superordinate frame or reference can have its origin, for example, in the center of mass of the Earth, the solar system, or locally, such as a small-scale coordinate system on a construction site with a defined coordinate origin. The axes can be given e.g. by the north or east direction, and the coordinate system can be correspondingly complementarily defined.

The description of a coordinate system is necessary for the transformation between the two coordinate systems. In this case, both coordinate systems can be expressed by each other, and there is no prioritization towards the superordinate coordinate system. Thus, in positioning tasks, the requirement arises that at least two coordinate systems are involved. Likewise, more than two coordinate systems can be involved.

In general, there are many different coordinate systems or their physical implementation as coordinate frames. With respect to the focus of this work, the emphasis is on local coordinate frames. Likewise, in the following test, the term "coordinate frame" is used since it concerns the realization of the coordinate system.

Groves (2013, pp. 27-28) describes a local coordinate frame having a local origin close to the area of interest. Usually, in local coordinate frames, the axis designation *North* (x-axis), *East* (y-axis) and *Down* (z-axis towards the center of the reference ellipsoid) are used, abbreviated as *NED*. The z-axis is often associated with the gravity vector. This allows simpler gravity models to be applied, even if they sometimes deviate slightly from the actual gravity values. However, other definitions are also used, such as *North-East-Up*, always under the conditions of a right-hand system. In the specific application in local positioning tasks, the local reference frame is usually realized as a local tangent plan,

i.e., at a point on the Earth's surface. As described, the x- and y-axes mostly align with directions such as North and East, and the z-axis with the normal to the plane through the origin. This reference frame also corresponds to the one in which measurements with a total station are performed.

Of great importance is the *body frame*. According to *Groves* (2013, p. 28-29) it is essential when interpreting the measurement data of the IMU sensors or using them for further calculations. The body frame is firmly connected to the respective carrier platform. During motion, there is no change in the coordinates of points expressed in this reference system.

2.2.2. Strapdown Inertial Navigation Systems

Strap-down systems are those that are firmly attached to the carrier platform.
Titterton & Weston (2004, p.3) describe this system as a combination of accelerometers and gyros. Further they delineate the advantages, such as lower costs, reduced weight, and increased reliability. The resulting computational requirements are addressed by the now-advanced capabilities in computer technology.

According to *Titterton & Weston* (2004, p.22 ff), consider a point P in a three-dimensional, fixed reference frame $_i$ described by the position vector $\boldsymbol{r}$ from the origin $\boldsymbol{O}$. The acceleration acting at point P is given by the second derivative of the position vector with respect to time (see eq. 2.1).

$$\boldsymbol{a}_i = \left(\frac{d^2\boldsymbol{r}}{dt^2}\right)_i \tag{2.1}$$

The measurement of the specific force $\boldsymbol{f}$ for a triad of perfect accelerometers, which also accounts for the gravitational vector $\boldsymbol{g}$, is given by eq. 2.2.

$$\boldsymbol{f} = \left(\frac{d^2\boldsymbol{r}}{dt^2}\right)_i - \boldsymbol{g} \tag{2.2}$$

A first integration yields to the velocity v_i of point P.

$$\boldsymbol{v}_i = \left(\frac{d\boldsymbol{r}}{dt}\right)_i \tag{2.3}$$

Additionally, a second integration gives the position vector.

The assumption of a stationary reference frame, however, is not realistic. If the reference system is in motion, the terms provided in 2.1 – 2.3 cannot be applied without additional

modifications. The following will present the equations (2.1 – 2.3) for motion in a frame that rotates with the Earth.
Depending on the choice of the reference frame, various factors, such as the rotation of the reference frame due to Earth's rotation, must be considered. The following discussion assumes an Earth-fixed frame. *Titterton & Weston* (2004, p. 30) describe a reference frame with its origin, for instance, in a tracking station (for missile applications), with axes aligned with the local vertical and a plane tangential to the Earth's surface at that point.
Further, *Titterton & Weston* (2004, p. 26 ff) describe the rate of change of v_e in the inertial frame as follows:

$$\left(\frac{d\boldsymbol{v}_e}{dt}\right)_i = \boldsymbol{f} - \boldsymbol{\omega}_{ie} \times \boldsymbol{v}_e + \boldsymbol{g}_l \tag{2.4}$$

where $\boldsymbol{v}_e$ represents the ground speed of an object in the Earth frame $_e$ and $\boldsymbol{\omega}_{ie}$ describes the rotation of the Earth Frame. Further, $\boldsymbol{g}_l$ is the local gravity vector. The change of $\boldsymbol{v}_e$ with respect to the Earth axes is given by:

$$\dot{\boldsymbol{v}} = \boldsymbol{C}_b^e \, \boldsymbol{f}^b - 2\boldsymbol{\omega}_{ie}^e \times \boldsymbol{v}_e^e + \boldsymbol{g}_l^e \tag{2.5}$$

Here, $\boldsymbol{C}_b^e$ represents the transformation of the measured specific force vector from the body to Earth frame.

$$\dot{\boldsymbol{v}}_e^e = \boldsymbol{C}_b^e \, \boldsymbol{f}^b + \boldsymbol{g}_l^e \tag{2.6}$$

For short-term navigation, simplifications regarding Earth's rotation can be made. Consequently, *Titterton & Weston* (2004, p. 30) provide a simplified form of the navigation equation shown in eq. 2.6.

2.2.3. Inertial Measurement Unit

2.2.3.1. Functional Principle

Inertial sensors have been an essential component of navigation solutions for many decades, particularly in aviation, space exploration and maritime navigation. As described by *Groves* (2013, p. 16 - 17), technological advancements have led to the production of increasingly compact sensors that are easy to manufacture and therefore cost-effective. The combination of various sensors in IMU has expanded the applications of inertial navigation, providing a reasonable, compact, and easy-to-install solution for various industries.

Groves (2013, p.16) defines, that inertial sensors are referred to when they do not rely on an external reference.
Essentially, IMUs are a combination of accelerometers and gyroscope triads. In some cases, additional sensors such as magnetometers may also be included. In most cases, there are at least three of each type of sensors present to enable a three-dimensional navigation solution. When referring to an IMU, it almost always involves a strap-down system. In this configuration, the inertial sensors are rigidly attached to the casing, thus following the motion of the platform.
For completeness, it should be noted that in contrast to strap-down systems, there are also inertial systems with gimbal stabilization. In this variant, the sensor does not follow the motion but is held in a stabilized position by actuators. The energy expended by the actuators serves as a measured quantity and is converted into accelerations and angular rates. However, this thesis is limited to strap-down systems.

Modern IMUs mainly consist of micro-electromechanical system (MEMS) sensors. MEMS is generally a term encompassing components that arise from the combination of mechanical and/or electronic sub-components and are produced in small sizes. It is neither a specific production technique or manufacturing process, nor is it a standalone product itself. *Titterton & Weston* (2004, p. 2013) explain in more detail different types of MEMS based IMUs as well as their different functional principles.
The microchips are very small ($<1\mu$m) but can still include various sensors, other electronical or mechanical components. Depending on the sensor, the measurements methods are based on different mechanical, optical, as well as chemical or biological processes. In integrated circuits, multiple components are then combined into an electronic circuit on a chip. This so-called system-on-a-chip technology enables a wide variety while maintaining minimal size as well as other advantages such as low power consumption and low production costs. Therefore, it is state-of-the-art in a wide range of applications today, such as smartphones or vehicles.
MEMS enable the transformation of incoming measurement signals into parameters, which can subsequently be further processed into a target parameter. The small size allows for short data processing paths, thereby minimizing latency effects and data loss. However, a frequently lower measurement accuracy, especially in the lower price segment, is to be considered critically. *Titterton & Weston* (2004, p. 189 - 192) as well as Groves (2013: p. 137 ff) discuss the advantages and disadvantages, but give as well an assessment on the accuracy aspect of MEMS.
Bosch [1], according to their website one of the leader in sensor technology, describes, that the production processes resemble those of semiconductors. A photolithographic layer is

[1] https://www.bosch.com/stories/topics/mems-micro-electro-mechanical-systems (access: August 2024)

applied to thin silicon layers, and structures are then imprinted through exposure and/or etching procedures. In a further step, movable parts can be incorporated. The production requirements are very high due to the small size alone and require low tolerances.

For acceleration measurement in MEMS, two different methods are commonly applied: vibration or a pendulum mass (mass-spring system).

Vibrating-beam Accelerometer

In *Groves* (2013, p.142), a vibrating-beam accelerometer is described as module with a stabilized proof mass, which is attached by two beams along the sensitive axis. These beams are electronically brought to vibration at their resonance frequency. If an external acceleration is applied to the sensor, the vibration frequency is accordingly changed. Compression of the beams leads to a decrease in frequency, while expansion leads to an increase in frequency. As shown in fig. 2.6, a double execution of the proof mass and the beams can also be present, leading to improved performance.

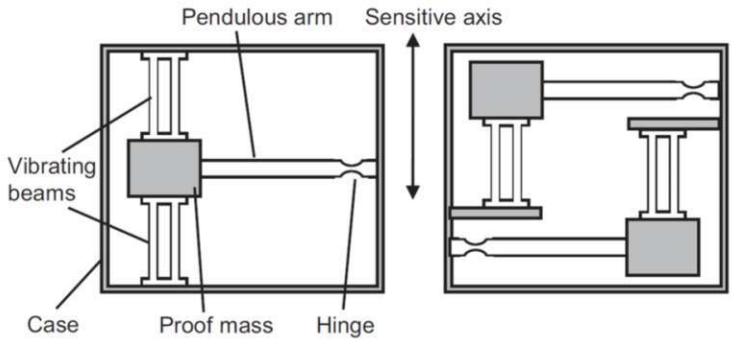

Figure 2.6: Functional principle of vibrating-beam accelerometers (*Groves* 2013, p. 142)

Pendulum Mass Accelerometer

In a pendulum accelerometer, there are two approaches in implementation, as described by *Groves* (2013, p. 141). In the open-loop configuration, the proof mass is freely oscillating and connected to the casing via a pendulum arm. The force exerted along the sensitive axis is transmitted to the pendulum arm via springs. A pick-off in the vicinity of the proof mass then measures the deflection. However, this design also brings disadvantages, such as the nonlinearity of the spring or the deviation of the sensitive axis in reference to the casing due to motion.

Therefore, for more precise MEMS accelerometers, there is the closed-loop (or force-back) configuration. In this configuration, the pendulum arm is held with the proof mass between two polarized permanent magnets via an electromagnet known as a torquer.

At the capacitive pick-off, a constant capacitance is measured on both capacitor plates. When an external force is exerted along the sensitive axis, the pendulum arm deflects towards one of the capacitors at the pick-off. Deflection of the pendulum arm leads to a larger capacitance at the capacitor closer to the pendulum arm, and vice versa, to a smaller capacitance at the more distant capacitor. The torquer counteracts the deflection and brings the pendulum arm back to the equilibrium position. Fig. 2.7 visualizes this principle. The energy expended for the restoration in the torquer is proportional to the applied force along the sensitive axis and thus constitutes the measurement quantity. The advantage lies in a constantly maintained alignment of the sensitive axis with reference to the casing and an increased range. There is also better linearity behaviour. However, a disadvantage is the greater sensitivity to damage, for example during transport. If the sensor is without power, there is no compensation for pendulum deflections, which can lead to damage of the components.

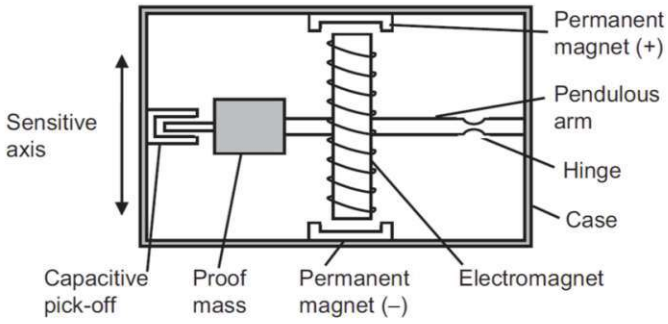

Figure 2.7: Functional principle of force-back pendulum accelerometer (*Groves* 2013, p. 141)

Vibrating Gyroscope

Gyroscopes are divided into two different technologies: optical gyros and vibrating gyros. This work focuses only on vibrating gyros, as there are primarily used in MEMS IMUs or implemented with MEMS technology.

Vibrating gyros observe the Coriolis acceleration of a vibrating component during the rotation of the gyro. This component can be configured differently, for example, as a ring, cylinder, beam or string. In this process, the corresponding component is set into a constant vibration. *Groves* (2013, p.147) describes the operating principle using a vibrating string. This string vibrates with a constant oscillation. When a rotation about the input axis (orthogonal to the virbation axis (drive axis), see fig. 2.8) is performed, the Coriolis force induces a harmonic motion along the output axis. The amplitude of this displacement is proportional to the angular velocity. Rotation about the drive axis

does not result in any displacement or generate any Coriolis acceleration.

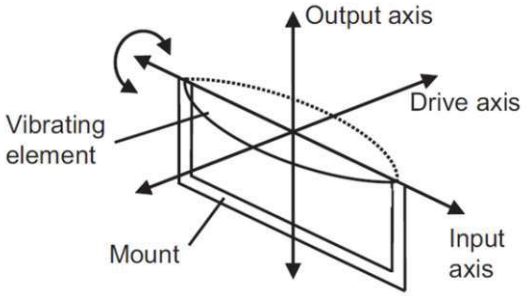

Figure 2.8: Functional principle of a vibrating string gyro (*Groves* 2013, p. 147)

Especially in the low-cost segment of MEMS gyros, the problem may arise that due to the structure, the vibration of the Coriolis acceleration is often very weak. As a result, the displacement is detected only with difficulty and not with sufficient accuracy.

2.2.3.2. Error Characteristics

In section 2.2.3.1, the functionality of IMUs was described, allowing for a closer examination of the error characteristics in the following chapter now. Figure 2.9 illustrates the schematic structure provided by *Groves* (2013, p.149).

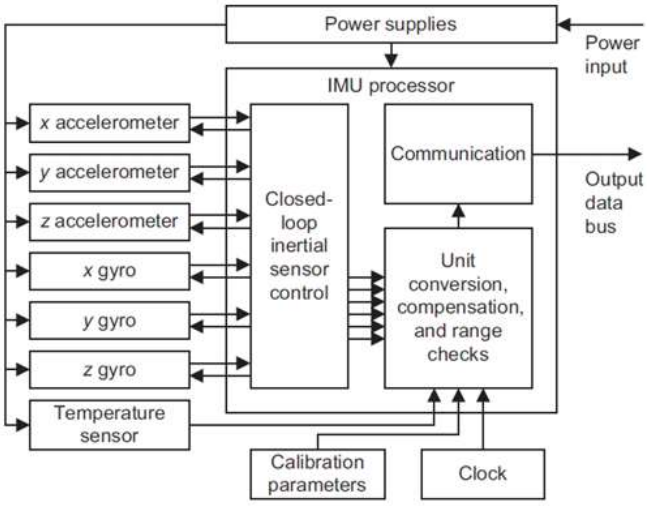

Figure 2.9: Structure of an IMU (*Groves* 2013, p. 148)

Groves (2013, p. 148) describes the processing unit as a component, where the respective sensor outputs are converted into angular rates and specific force. The specific force in this context does not describe force in the literal sense, but rather acceleration. This arises from the fact that in an (unaccelerated, non-rotating) inertial reference frame, there is no

gravitational field prevailing. Thus, the inertial force per unit mass corresponds to the acceleration of the mass.
Furthermore, the processing unit also houses the calibration parameters. These compensate for constant errors and are determined under laboraty conditions over a specified temperature range, as the errors are temperature-dependent. Temperature influences are accordingly compensated by the internal temperature sensor in combination with temperature calibration parameters. If temperature dependence is not considered, larger deviations can be expected, especially during the initial warming-up phase after start.

When looking onto the error characteristics, there exist different sources which sum up to an overall error. In *Groves* (2013, p.151), this overall error is subclassified into four major components:

- **fixed component**: present in every application and compensated by calibration parameters.
- **temperature-dependent component**: compensated by calibration parameters and temperature sensor (if available).
- **run-to-run component**: varies with each application but is constant over the period of use. Cannot be compensated by calibration but can be handled with integration algorithms, for example.
- **in-run component**: slow variation over the period of IMU application. Cannot be corrected by calibration or alingment processes. Theoretically, the error can be determined through integration with additional navigation sensors, but it is difficult to observe.

Further, *Groves* (2013, p.149) gives a definition on the calibration parameters. They include accelerometer and gyro bias, scale factor and cross-coupling errors, as well as a bias depending on the g-vector. These will be briefly described below. Depending on accuracy level and application area, the parameters are determined once for an entire production series or, for special accuracy requirements, for each IMU. There is also a distinction between calibration in the laboratory or under on-site conditions during use, known as an in-run calibration.

Bias

The bias describes a constant error that is independent of the magnitude of the measured angular rate and specific force. *Groves* (2013, p.152) also describes a bias that exhibits a dependence on the specific force. However, the independent part is the larger component

IMU Grade	Accelerometer Bias		Gyro Bias	
	mg	$m\,s^{-2}$	$^\circ\,hr^{-1}$	$rad\,s^{-1}$
Marine	0.01	10^{-4}	0.001	5×10^{-9}
Aviation	0.03 – 0.1	$3 \times 10^{-4} - 10^{-3}$	0.01	5×10^{-8}
Intermediate	0.1 – 1	$10^{-3} - 10^{-2}$	0.1	5×10^{-7}
Tactical	1 – 10	0.01 – 0.1	1 – 100	$5 \times 10^{-6} - 5 \times 10^{-4}$
Consumer	> 3	> 0.03	>100	$> 5 \times 10^{-4}$

Figure 2.10: Different Grades of IMUs (adapted from *Groves* (2013, p. 154)), ranked by the accelerometer bias and gyro bias.

and is simultaneously the main component of the overall errors. Due to this significant portion, IMUs can be classified based on the bias. Figure 2.10 shows the a classification based on the accelerometer bias and the gyro bias.
The bias can be distinguished into two parts: a dynamic part b_d and and a static part b_s. The total bias is thus the sum of the static and dynamic parts (see eq. 2.7), where b_a describes the accelerometer bias and b_g the gyro bias:

$$\begin{aligned} b_a &= b_{a,stat} + b_{a,dyn} \\ b_g &= b_{g,stat} + b_{g,dyn} \end{aligned} \tag{2.7}$$

The static part (fixed bias) includes the run-to-run component and the residual fixed bias. The dynamic component represents the in-run error as well as the temperature-dependent bias and corresponds in magnitude to approximately 10% of the static part.

Scale Factor Error

As described by *Groves* (2013, p.154), the scale factor error reflects the distinction between the true sensitivity of the sensors and the sensitivity presumed during calibration. The error is proportional to the true specific force (accelerometer) and the true angular rate (gyro). Figure 2.11 visualizes the scale factor error with reference to input and output.

Further *Groves* (2013, p. 158) writes, that a problem regarding the scale factor error is its deviation from the (ideal) linearity. This non-linearity occurs when the scale factor varies over the entire operating range of specific force and angular rate. The strongest effect of this influence is usually observed in the maximum areas of the individual sensors' operating range.

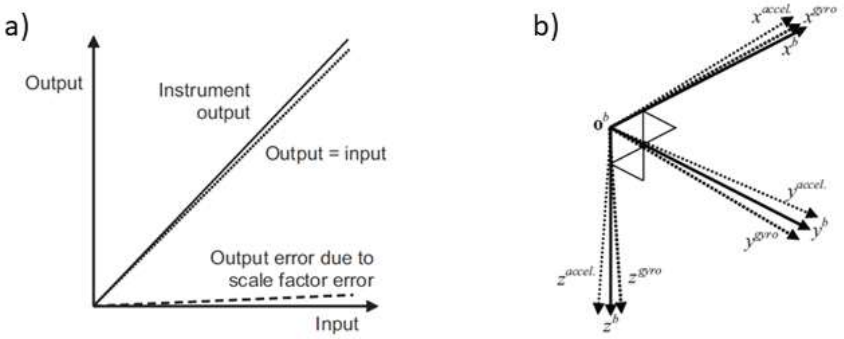

Figure 2.11: Visualization of *scale factor error* (figure *a*) and the *cross-coupling error* (figure *b*) (*Groves* 2013, p. 154)

Cross-Coupling

Groves (2013, p. 154) characterises cross-coupling or misalignment as errors, that arise from the deviation of the sensitive axes of the intertial system ($_{accel.}$ and $_{gyro}$ in fig. b in 2.11) from the orthogonal system of the body frame ($_b$ in fig. b in 2.11). This results in the specific force measured along one axis also containing influences from the other orthogonal axes. It can be assumed that the lower the grade of the IMU (see fig. 2.10), the greater the influence of cross-couplings due to the lower production accuracy.

Groves (2013, p.155) combines the scale factor error and the cross-coupling error in matrix notation (see 2.8), separated in accelerometer (M_a) and gyro (M_g):

$$M_a = \begin{pmatrix} s_{a,x} & m_{a,xy} & m_{a,xz} \\ m_{a,yx} & s_{a,y} & m_{a,yz} \\ m_{a,zx} & m_{a,zy} & s_{a,z} \end{pmatrix} , \; M_g = \begin{pmatrix} s_{g,x} & m_{g,xy} & m_{g,xz} \\ m_{g,yx} & s_{g,y} & m_{g,yz} \\ m_{g,zx} & m_{g,zy} & s_{g,z} \end{pmatrix} \tag{2.8}$$

$m_{a,g}$ describe the cross-coupling coefficient between the indicated axes and $s_{a,g}$ the scale factor error along the axes.
M_a and M_g are unitless and typically range from 10^{-3} to 10^{-4}. However, this value can increase up to 0.1 in uncalibrated MEMS IMUs. In contrast, in ring laser gyros, both errors (scale factor, cross-coupling) range from 10^{-4} to 10^{-6} (see fog. 2.10).

Random Noise

This effect is present in every IMU and mainly consist of a white noise component and a high-frequency component. According to *Groves* (2013, p. 156), it can have various causes, including electrical or mechanical factors as well as vibrations. Depending on the measurement principle, the sensors are influenced to different extents by the noise.
For example, in MEMS sensors, it tends to have a stronger impact on the measurements,

especially when the sensor signal is weak. In this design, very high-frequency noise can also occur. Generally, the effect can be eliminated by applying navigation equations, with the limitation that the IMU must remain stationary. In the case of a moving IMU, the effect is only reduced but not eliminated. Alternatively, filters can also provide relief, such as the application of a low-pass filter or a dynamic bandpass filter, which adjusts itself according to the level of motion.

Other Errors

There are various other error causes, which can be found in more detail in *Groves* (2013, p. 159). The most important are briefly described in the following paragraph.

Another error that can be compensated by calibration is the so-called size effect. This describes the deviation of the individual sensor axes from the IMU reference point. This error only affects the acceleration measurement since rotation around the axis is independent of the reference point and is therefore not determined for every IMU.

The influence of vibration should also be briefly mentioned. In an environment where virbations prevail, these can also have a negative impact on the inertial sensor. Especially when the vibration frequency is similar to one of the resonance frequencies or the update rate of the processing unit, this manifests itself similarly to a bias in the error budget. MEMS sensors are particularly susceptible to this effect, as phenomena such as nonlinearity tend to be more pronounced. Additionally, filters (low-pass) used to suppress high-frequency noise exacerbate the influence, resulting in an overall increase in noise.

INS Error Propagation

Groves (2013, p.203) describes three sources of errors related to INS:

1. Accelerometer and gyro measurements
2. Initialization errors
3. Approximations in processing

Further *Groves* (2013, p. 203) describes that the integration of the biases from the accelerometer and gyro leads to increasing errors in position, velocity and attitude over time. The initial velocity error results in an increasing position error. The inherent limitations of the navigation equations, along with the random noise from the accelerometer and gyro, collectively worsen the errors in the navigation solution. Furthermore, errors in attitude impact both velocity and position. The position errors feeding back into the system through the gravity model, both positvely and negatively.

Error propagation in INS is described as very comprehensive and complex even in the literature. For a more detailed description of error propagation in inertial measurement systems, reference is made to the literature, such as *Groves* (2013, p.203 ff).

2.2.3.3. IMU Initialization

The navigation solution is calculated by integrating measurements from the inertial sensors. In the navigation equations, previous measurements are therefore also used, which are not yet available at the very beginning. For this, the algorithm now requires an initial position and an initial attitude solution. These can be determined externally, or in the case of attitude initialization, an initial solution can also be calculated by measuring gravity and Earth rotation. External sources that can provide a position solution include GNSS or a total station, but many other solutions can be found in the literature (i.e. Groves (2013), p.197).

However, since the underlying algorithm for the initialization of the AP20 AutoPole's INS is not disclosed, an attempt is made to describe it as accurately as possible using approaches found in the literature. The initialization of the AP20 AutoPole involves the commencement of continuous measurements of the prism position, followed by necessary movements of the pole or the AP20 AutoPole itself.

Groves (2013, p. 627ff) describes a similar process known as transfer alignment. In this procedure, the INS is initialized, aligned, and calibrated while in motion.

Therefore, *Groves* (2013, p. 628) outlines three phases, with Phase 3 involving a re-initialization process, which, as described in the referenced literature, is conducted shortly before the launch phase of the example flight object. This phase is not present in the AP20 AutoPole system. For a more in-depth explanation, reference is made to the previously mentioned section in *Groves* (2013, p. 628).

Returning to the phases, the process begins with the so-called "one shot" initialization, where the INS is aligned with the position, velocity, and attitude solution of the reference navigation system. In the subsequent measurement-matching phase, the navigation solutions from both the INS and the reference system are combined and compared within a Kalman filter. This comparison allows for the derivation of corrections to the navigation solution and facilitates the calibration of IMU parameters.

Additionally, *Groves* (2013, p. 629) describes various methods for conducting transfer alignment. One such method is conventional measurement matching, where either the position or the velocity is used, but never both simultaneously, as they are correlated through time integration. This method results in linear measurement matching. In contrast, the rapid transfer alignment method includes an attitude measurement matching in addition to the conventional transfer alignment. The advantage of rapid transfer align-

ment lies in its shorter duration for determining attitude errors, though a longer period is still required for identifying IMU errors. Another benefit is that it does not require specific maneuvers for initialization, unlike the conventional transfer alignment method. In general, the literature, such as *Groves* (2013) and *Titterton & Weston* (2004), provides detailed definitions of many other initialization methods. However, since the exact initialization algorithm of the AP20 AutoPole is not known, only a few example methods have been mentioned here. A comprehensive description of all possible methods would exceed the scope of this work. Therefore, the reader is referred to the mentioned literature for further details.

3. Tilt Compensation

3.1. IMU-based Tilt Compensation

Determining the attitude of an object denotes the determination of an object's orientation with respect to a reference frame. Presently, the computation of an object's three-dimensional orientation finds widespread application across diverse entities navigating through space. Leveraging the high sampling rates provided by MEMS IMUs, a notably high-resolution calculation of attitude is achievable, facilitating swift sensor response during Unmanned Aerial Vehicle maneuvers or algorithmic interventions for motion correction and stabilization, as exemplified by robots like *Boston Dynamics' Spot*.
Sensor fusion algorithms combine various sensor data inputs and manage diverse influences such as bias, enabling efficient real-time data processing on the onboard processor without external computational dependencies.
Traditionally, three fundamental methods have become established for attitude determination:

1. Euler Angles
2. Coordinate Transformation Matrix, Direction Cosine Matrix
3. Quaternion

In the following, lower and upper indices are employed for the description of coordinate systems. It is specified that the lower index denotes the original coordinate frame, while the upper index denotes the target coodinate frame.
Furthermore, $\boldsymbol{C}$ is used to describe a rotation matrix.

3.1.1. Euler Angles

Euler angles, named after the Swiss mathematician *Leonhard Euler*, are foundational in the representation of an object's orientation in three-dimensional space due to their inherent simplicity and intuitive nature. As implied by their nomenclature, Euler angles describe rotations around specific axes. They articulate the spatial orientation of an object by delineating the rotation of a typically body-fixed coordinate system with respect to a local navigation frame. This mathematical construct essentially encapsulates a sequence of rotational transformations. In scholarly discourse, Euler angles are frequently denoted as ϕ, θ and ψ or referred to as *Roll*, *Pitch* and *Yaw*. The term *Heading* is often used interchangeably with Yaw.

While six possible rotation variants exist in theory, attention here is directed towards elucidating the principles underlying the so-called *Tait-Bryan* angle convention. *Groves* (2013, p.34) characterizes the successive rotation sequence with the order: *z-y-x* (shown by equation 3.1).

$$\boldsymbol{R}_{\boldsymbol{b}}^{\boldsymbol{n}} = \boldsymbol{R}_{\boldsymbol{b},\boldsymbol{z}}^{\boldsymbol{n}}(\boldsymbol{\psi})\, \boldsymbol{R}_{\boldsymbol{b},\boldsymbol{y}}^{\boldsymbol{n}}(\theta)\, \boldsymbol{R}_{\boldsymbol{b},\boldsymbol{x}}^{\boldsymbol{n}}(\phi) = \tag{3.1}$$

$$= \begin{pmatrix} cos\,\psi_b^n & sin\,\psi_b^n & 0 \\ -sin\,\psi_b^n & cos\,\psi_b^n & 0 \\ 0 & 0 & 1 \end{pmatrix} \begin{pmatrix} cos\,\theta_b^n & 0 & -sin\,\theta_b^n \\ 0 & 1 & 0 \\ sin\,\theta_b^n & 0 & cos\,\theta_b^n \end{pmatrix} \begin{pmatrix} 1 & 0 & 0 \\ 0 & cos\,\phi_b^n & sin\,\phi_b^n \\ 0 & -sin\,\phi_b^n & cos\,\phi_b^n \end{pmatrix}$$

It is observed that Euler angles are influenced by the order of rotation, and altering the sequence of rotations can yield distinct outcomes. However, Euler angles are barely employed in attitude determination due to a fundamental limitation known as *Gimbal Lock*. This phenomenon arises when the Pitch equals 90 [°], resulting in a reduction in degress of freedom. Consequently, Roll and Yaw become dependent on each other, diminishing their independence. The lost degree of freedom in practice means the ability to rotate around an axis is lost. This is primarily due to the dependence of Euler angles on the order of rotations. In contrast, quaternions describe rotation not as a sequence of rotations but as a single entity. In the AP20, quaternions are used in the attitude determination to overcome the Gimbal lock phenomenon.

Coordinate Transformation Matrix, Direction Cosine Matrix

Another form to describe the orienation by Euler angles is the coordinate transformation matrix, also referred to as direction cosine matrix.

A coordinate transformation matrix is a mathematical construct represented by a 3x3 matrix. It serves the purpose of converting vectors from one coordinate system to another

by means of matrix multiplication with the corresponding transformation matrix, as shown in eq. 3.2:

$$\boldsymbol{x}^{\beta} = \boldsymbol{C}_{\alpha}^{\beta}\, \boldsymbol{x}^{\alpha} \tag{3.2}$$

As illustrated by *Groves* (2013, p.36, eq. 2.13), the components of the coordinate transformation matrix are derived from the product of the unit vectors along the respective axes of both the source and target frames. This product effectively yields the cosine of the angle between the corresponding axes, thus justifying the terminology *direction cosine matrix* commonly found in the literature. Equation 3.3 explains the structure of the matrix:

$$\boldsymbol{C}_{\alpha}^{\beta} = \begin{pmatrix} \boldsymbol{u}_{\beta x} \cdot \boldsymbol{u}_{\alpha x} & \boldsymbol{u}_{\beta x} \cdot \boldsymbol{u}_{\alpha y} & \boldsymbol{u}_{\beta x} \cdot \boldsymbol{u}_{\alpha z} \\ \boldsymbol{u}_{\beta y} \cdot \boldsymbol{u}_{\alpha x} & \boldsymbol{u}_{\beta y} \cdot \boldsymbol{u}_{\alpha y} & \boldsymbol{u}_{\beta y} \cdot \boldsymbol{u}_{\alpha z} \\ \boldsymbol{u}_{\beta z} \cdot \boldsymbol{u}_{\alpha x} & \boldsymbol{u}_{\beta z} \cdot \boldsymbol{u}_{\alpha y} & \boldsymbol{u}_{\beta z} \cdot \boldsymbol{u}_{\alpha z} \end{pmatrix} = \begin{pmatrix} cos(\mu_{\beta x,\alpha x}) & cos(\mu_{\beta x,\alpha y}) & cos(\mu_{\beta x,\alpha z}) \\ cos(\mu_{\beta y,\alpha x}) & cos(\mu_{\beta y,\alpha y}) & cos(\mu_{\beta y,\alpha z}) \\ cos(\mu_{\beta z,\alpha x}) & cos(\mu_{\beta z,\alpha y}) & cos(\mu_{\beta z,\alpha z}) \end{pmatrix} \tag{3.3}$$

It is possible to convert a coordinate transformation matrix to Euler angles and vice versa. Equation 3.4 illustrates this relationship for determining the Euler angles from the rotation matrix:

$$\begin{aligned} \phi_{\beta\alpha} &= arctan_2(\boldsymbol{C}_{\beta\,2,3}^{\alpha},\, \boldsymbol{C}_{\beta\,3,3}^{\alpha})\,, \\ \theta_{\beta\alpha} &= -arcsin(\boldsymbol{C}_{\beta\,1,3}^{\alpha})\,, \\ \psi_{\beta\alpha} &= arcta_2(\boldsymbol{C}_{\beta\,1,2}^{\alpha}),\, \boldsymbol{C}_{\beta\,1,1}^{\alpha}) \end{aligned} \tag{3.4}$$

3.1.2. Quaternion

Quaternions are used to represent the spatial orientation of an object. In contrast to Euler angles, however, three censecutive rotation angles are not used. Instead, the representation is in the form of a four-part complex number, as follows:

$$q = w + xi + yj + zk \tag{3.5}$$

When applying quaternions to orientation determination, the gerneral form as in eq. 3.5 takes the following form:

$$q = cos\left(\frac{\omega}{2}\right) + \boldsymbol{V}_{Rot}\, sin\left(\frac{\omega}{2}\right) = \tag{3.6}$$

$$= cos\left(\frac{\omega}{2}\right) + V_x\, sin\left(\frac{\omega}{2}\right) i + V_y\, sin\left(\frac{\omega}{2}\right) j + V_z\, sin\left(\frac{\omega}{2}\right) k$$

where i, j, k represent the unit vectors of the Cartesian axes and ω is the rotation angle. Further this means that $cos\left(\frac{\omega}{2}\right)$ only depends on the magnitude of the rotation, but the other elements in 3.6 depend on the magnitude of the rotation as well as the axis of rotation.
Quaternions offer many advantages when applied in attitude determination. They are more efficient and stable in calculation and, for example, offer the advantage over Euler angles that they are easier to handle as well as independent of the previously explained *Gimbal Lock*. However, they are also less intuitive and less visually straightforward than Euler angles.

3.2. Pole Tilt Compensation Calculations

The previously discussed fundamentals form the basis of pole tilt compensation.
Interest in tilt compensation in the context of geodetic measurements is not a new problem. As mentioned at the beginning of this thesis, the compensation of pole tilts is already widely applied in GNSS measurement systems (see, for example, *Luo et al.* (2018)). The underlying issue is that for precise point determination — whether using RTK-GNSS or a total station with a survey pole — the pole must be positioned and stabilized in a vertical orientation, aligned with the local vertical direction.
However, this task cannot be accomplished entirely without residual errors. As a result, this unknown error propagates into the point determination, and the magnitude of the error at any given time remains unknown and therefore cannot be compensated for. Furthermore, if no stabilization of the pole, such as by using a bipod, is performed, this unknown error varies over time or the duration of the measurement with a likewise unknown magnitude.
To address this problem, it is necessary to have high-resolution measurement data available, at least during the actual measurement period (for example when using a total station) to compensate for the previously described unknown residual tilt.
The problem described above thus leads to the requirements for such a system. It should allow for highly frequent and high-resolution tilt measurements, be as compact as possible, and be robust enough to operate reliably within a modern geodetic measurement system under various external conditions. The specific technical aspects and their implementation in a product are described in detail in section 3.3. This chapter now focuses on the functional solution to the initially mentioned problem, with an emphasis on geodetic measurements using a prism with a total station.

Since this is a highly specialized field, it has been rarely addressed in the literature and publications. Reference can be made here to a publication by *Maar* (2022), which specif-

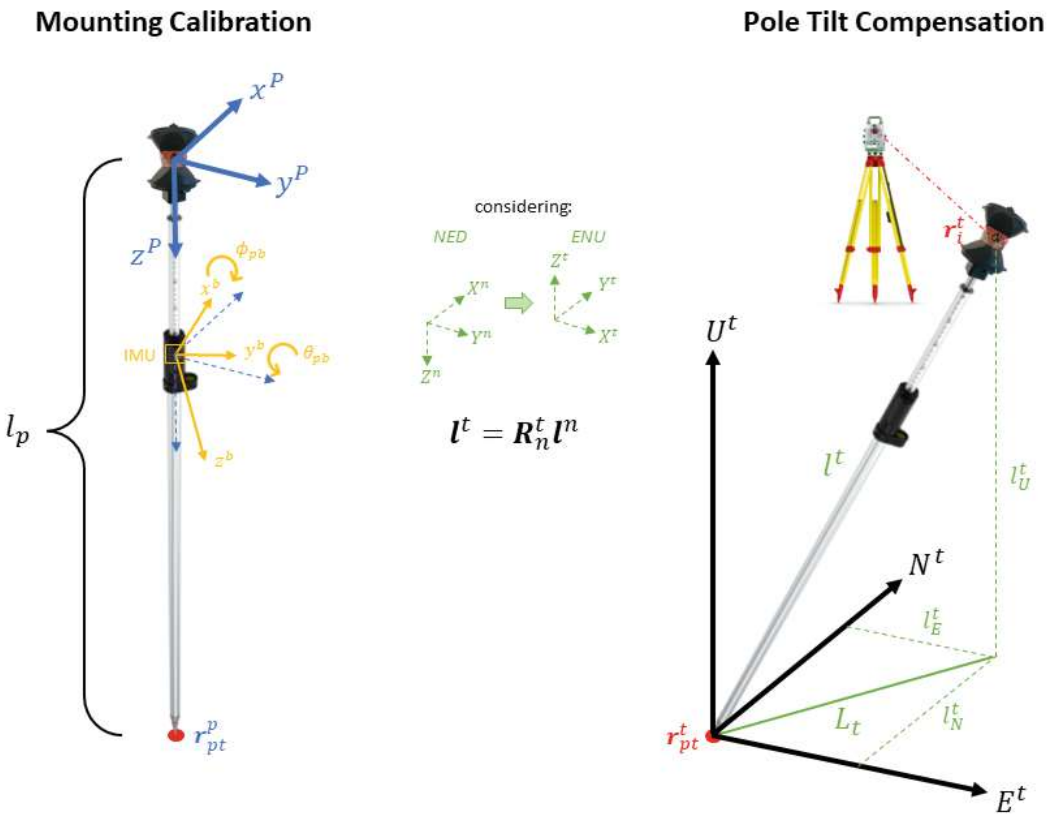

Figure 3.1: Principle of mounting calibration and pole tilt compensation (adapted from *Thalmann et al.* (2020, p. 4))

ically focuses on the AP20 AutoPole as a product, and will be discussed in more detail later in section 3.3. However, *Thalmann et al.* (2020) have explored the methodology and specific application of tilt compensation for poles in connection with total stations in detail. It should be noted here that, despite the focus on accelerometer data in this publication, the underlying methodology of pole tilt compensation can still be explained based on the work of *Thalmann et al.* (2020).

In general, pole tilt compensation involves a series of transformations between different coordinate frames. The ultimate goal is to determine the coordinates of the ground point corresponding to the tip of the pole. The principle is visualized in fig. 3.1.
Thalmann et al. (2020, p. 4) begin at the sensor level. The sensor output consists of the specific force $\boldsymbol{f}_s = [f_{x,s}\,,\, f_{y,s}\,,\, f_{z,s}]$ measured along the individual axes in the non-orthogonal sensor frame denoted by $_s$. As shown in eq. 3.7, this vector $\boldsymbol{f}_s$ is composed of the vector of calibrated forces $\boldsymbol{f}^a$, the bias vector $\boldsymbol{b}_f$, the random noise $\boldsymbol{v}_f$ from the accelerometer, and a scale factor matrix $\boldsymbol{S}_f$.

$$\boldsymbol{f}_s = \boldsymbol{S}_f\, \boldsymbol{f}^a + \boldsymbol{b}_f + \boldsymbol{v}_f \tag{3.7}$$

The sensitive axes are non-orthogonal due to inaccuracies, i.e. during sensor installation, necessitating a rotation into the orthogonal body frame $_b$. The rotation $\boldsymbol{T}_a^b$ can be simplified due to the small angles involved:

$$\boldsymbol{f}^b = \boldsymbol{T}_a^b \, \boldsymbol{f}^a, \quad with \;\; \boldsymbol{T}_a^b = \begin{bmatrix} 1 & -\alpha_{yz} & \alpha_{zy} \\ 0 & 1 & -\alpha_{zx} \\ 0 & 0 & 1 \end{bmatrix} \tag{3.8}$$

In the next step, *Thalmann et al.* (2020, pp. 5-6) introduce the so-called IMU leveling. As shown in eq. 3.9, this process involves determining the Euler angles roll ϕ_{nb} and pitch θ_{nb}. The notation $_{nb}$ is used because the leveling process aligns the IMU body frame $_b$ with respect to the local navigation frame $_n$. The $arctan()$ in the roll computation is only valid when the tilt is limited to the upper half sphere, where the tilt angle is between 0° and 90°. If a higher tilt angle is examined, $arctan()$ needs to be replaced by $arctan_2()$.

$$\phi_{nb} = atan(-f_y^b, -f_z^b) \;, \;\; \theta_{nb} = atan\left(\frac{f_x^b}{\sqrt{f_y^{b2} + f_z^{b2}}}\right) \tag{3.9}$$

Another important aspect is the relationship between the IMU's body frame, located somewhere on the pole, and the pole frame $_p$ itself (see eq. 3.10). This rotation of the body frame into the pole frame can be described using Euler angles via a transformation matrix $\boldsymbol{C}_b^p$. The principle is shown in fig. 3.1

$$\boldsymbol{C}_b^p = \boldsymbol{C}_b^p(\phi_{pb}, \theta_{pb}) \tag{3.10}$$

The relationship between the two reference frames $_b$ and $_p$ is determined in advance through calibration. *Thalmann et al.* (2020, p. 8) describes a calibration routine where the pole is placed on a known coordinate point $\boldsymbol{r}_{pt}^t$ and then tilted. To determine the parameters, the condition from eq. 3.11 must be fulfilled.

$$\boldsymbol{r}_i^t + \boldsymbol{R}_n^t \, \boldsymbol{l}^n - \boldsymbol{r}_{pt}^t = 0 \tag{3.11}$$

As shown in fig. 3.1, the term $\boldsymbol{r}_i^t$ is a prism measurement by the total station and $\boldsymbol{R}_n^t$ transforms the pole vector $\boldsymbol{l}^n$, given in the navigation frame, to the total station's frame, denoted by $_t$. The composition of $\boldsymbol{R}_n^t$ is shown in eq. 3.15.
This condition can be simplified to the horizontal displacement L of the prism. In eq. 3.12, the term $L^{'}$ is determined through observations from the total station, while L is derived from IMU measurements.

$$\sqrt{n^{'\,2} + e^{'\,2}} - \sqrt{n^2 + e^2} = L^{'} - L = 0 \tag{3.12}$$

The pole is described by a vector l^p, where l_p is the pole length from prism center to the pole tip:

$$l^p = \begin{bmatrix} 0 \\ 0 \\ l_p \end{bmatrix} \tag{3.13}$$

In a final transformation step, the pole frame is rotated into the local horizontal navigation frame using equation 3.14.

$$l^n = \boldsymbol{C}_p^n \boldsymbol{l}^p = \boldsymbol{C}_b^n \boldsymbol{C}_p^b \boldsymbol{l}^p \tag{3.14}$$

Thus, $\boldsymbol{l}_n$ represents the coordinate components of the tilted pole within the navigation frame.

The calculation of the coordinates of the ground point $\boldsymbol{r}_{pt}^t$ is given by eq. 3.15. Usually, the before mentioned frames (body, pole, navigation) are defined as a North-East-Down (NED) System. In contrast, the system of the total station, referred to as the t frame by *Thalmann et al.* (2020, p. 6), is typically an East-North-Up (ENU) system. Therefore, a conversion between these two system is necessary, done by R_n^t. Additionally, a measurement r_i^t to the prism mounted on top of the pole is necessary. Figure 3.1 already takes care of the mentioned conversion to the ENU frame.

$$\boldsymbol{r}_{pt}^t = \boldsymbol{r}_i^t + \boldsymbol{R}_n^t \boldsymbol{l}^n \quad , with \;\; \boldsymbol{R}_n^t = \begin{bmatrix} 0 & 1 & 0 \\ 1 & 0 & 0 \\ 0 & 0 & -1 \end{bmatrix} \tag{3.15}$$

3.3. *Leica Geosystems* AP20 Autopole

By the description of what and how a total station works, one can see that these devices support the surveyors in many aspects. The on-site work and tasks changed over time and led the focus of the user from manual workflows to the software and the usage of modern features, applications and functionalities within it. Nevertheless, many user actions still have influence on the measurement and further on the result. One example is a wrong target height that leads to a wrong z-component in the derived coordinates.

To overcome avoidable user errors, Leica tracked down potential ways to avoid them by implementing new sensors and software features. This resulted in the launch of the *AP20 AutoPole* in the year of 2022.

The manufacturer promises to reduce the risk of wrong target height (PoleHeight feature) and to lock to a wrong prism when using target tracking (TargetID feature). Furthermore, tilt compensated measurements were enabled and increase the accuracy (see *Leica*

Geosystems 2022 and *Maar* 2022).
In order to better understand the results shown later in this thesis, a theoretical description of the functionality and features are given in advance and the product is explained in more detail. At the beginning the hardware will be described. Afterwards the different functionalities and the workflow are described at the end of this section.

3.3.1. Design

With the launch the AP20 AutoPole, Leica released four variants of the device. Each variant has the same design and size, but the difference is given with their functionalities. In general, they can be divided into two groups: models that enable for tilt compensation ('AP20' and 'AP20 T'), and non-tilt variants ('AP20 H' and 'AP20 ID').
The functionalities available with which variant are shown in 3.2:

LEICA AP20 AUTOPOLE VARIANTS	AP20 H	AP20 ID	AP20 T	AP20
PoleHeight	✔	✗	✔	✔
Tilt Compensation[4]	✗	✗	✔	✔
TargetID[5]	✗	✔	✗	✔

Figure 3.2: Overview on the features of each AP20 AutoPole variant (Leica Geosystems 2021)

The device has a height of 187.9 mm including the antenna (136.2 mm without antenna) and a width of 94 mm. With attached battery the device weighs 0.5 kg. It is only possible to use batteries of type GEB321. These allows a usage of 16 hours for non-tilt variants and 6 hours for tilt variants according to the manufacturer. On one side the interface to operate the AP20 AutoPole is located (see 3.3, Left). This interface has one button to turn it on or off. Further there are three LED symbols, that show the user the battery status (right LED), the connection status (central LED) and the tilt status (left LED). The tilt status LED is not active when using a non-tilt variant.

Figure 3.3: Left: AP20 Autopole Interface with LED icons
Right: Battery compartment with USB-C interface and antenna

On the underside of the device, the antenna for TPS communication is positioned, along with the USB (Type C) slot for firmware loading as well as the battery compartment (see fig. 3.3, Right). The device is certified to meet the IP67 standard, indicating protection against solids and resistance to brief immersion in water.
Mounting the AP20 AutoPole, such as on the GLS51 pole, involves inserting the upper pole tip through the central opening of the AP20 AutoPole and then performing a twisting motion (either clockwise or counter-clockwise) to secure the AP20 AutoPole to the pole. To detach it, the button above the TargetID LED strip must be pressed to release the connection, allowing the AP20 AutoPole to be removed from the pole.

3.3.2. Feature: TargetID

The functionality is an extension to the common PowerSearch and is implemented by using a LED strip in the upper area of the AP20 AutoPole (see 3.4). This LED strip emits a unique signature resulting from the assigned identification number. Leica Captivate allows to choose between 16 different identifications. The signature is given by different pulse frequencies depending on the choosen ID.
Furthermore, this means that 16 AP20 AutoPole devices (with TargetID) can be used simultaneously on the same site.
If a PowerSearch is triggered by the user, the LED strip is activated and continuously radiates the previously assigned signature until the prism search was successful (see fig. 3.5). The trigger to activate the signature is send by the total station when starting a PowerSearch. While the total station does its horizontal turn, it searches within a +/- 20°

Figure 3.4: Target ID: LED strip showing unique signature

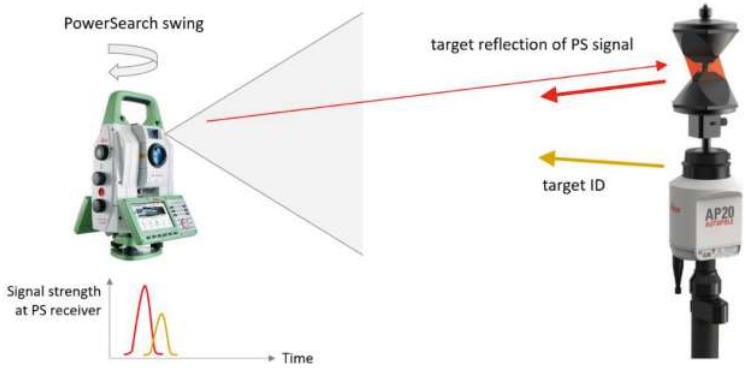

Figure 3.5: Target ID workflow (Maar 2022)

fence for the prism as well as the corresponding LED signature, that are expected to be next to each other. If this is the case and the PowerSearch receiver detects both signals (reflection from target and TargetID signature), the vertical ATR search is started and if successful, the LED strip is turned off afterwards.

3.3.3. Feature: PoleHeight

The PoleHeight function allows to automatically update the prism's height within Leica Captivate software. The technology behind the automatic reading of height is mounted inside the reflector pole. By attaching an AP20 AutoPole model that supports this feature to a pole (only compatible with GLS51, GLS51F, CRP4, CRP5), a passive electronic supply for the pole is build up which provides current for the electronic parts inside. To determine a height value, two elements are necessary: a static magnet, that is mounted at the handgrip and generates a small magnetic field and as a second part, so-called Hall sensors are equally distributed along the inner pole tube holes with a spacing of 5 cm. They are called Snaplock positions. The Hall sensors detect the nearby magnetic field everytime one of these positions is reached. By knowing the order of this Hall sensors as well as the dimension of the pole tube, a unique height value can be determined. NFC transmits the value to the AP20 AutoPole, which subsequently transfers it to the controller or total station. As can be seen, it is only possible to automatically update height values that are linked to the mentioned Snaplock positions. In between them, no automatic height reading is available and thus, the software cannot display the actual height. Here, the software will show dashes and for the case a measurement is triggered by the user at that time, a notification shows the missing height value. At any time, the operator is able to manually enter a height value and also to overrule the automatic reading where necessary. By changing the height to another or the same snaplock position (by only push the snaplock button), the automatic reading will be displayed again in the software.
The PoleHeight feature is available either for total station or GNSS products by Leica.

3.3.4. Feature: Tilt Compensation

This section shall give a short description of the tilt compensation functionality of AP20 AutoPole. Because the main focus of this thesis is on the tilt compensation variant of the AP20 AutoPole, the compensation is described in a separate section (see section 3.2). The AP20 AutoPole enables the user to have a real-time compensated coordinate shown in the software.

To get compensated coordinates, the user has to perform an initialization movement. This movement is necessary to calculate an inertial relative position and orientation, which enables the processing algorithm to accurately estimate its errors by its own observations. Thus, a proper performed initialization minimizes the tilt error and also the stability of the tilt status. In section 4 further details will be shown regarding initialization.
To use tilt compensation in real-time update of the coordinate requires a fast and stable communication between the TPS and the AP20 AutoPole. This is realized by Bluetooth Low Energy. Both, TPS and AP20 AutoPole possess a Bluetooth module. On TPS side an additional so-called Radio Handle (Radio Handle RH18) is needed (see section 2.1). The main challenge with using real-time tilt measurements lays in the synchronization of the different clocks within the multi-sensor system. Regarding AP20 AutoPole this means, that AP20 AutoPole's clock has to be synchronized to the total-station clock, where no physical connection is given. Depending on the used AP20 AutoPole variant, the communication path between total station and AP20 AutoPole differ only on the used Bluetooth type. For non-tilt variants, a common Bluetooth connection is established to transfer the height data or to trigger the TargetID.
Maar (2022) describes the communication path as follows:

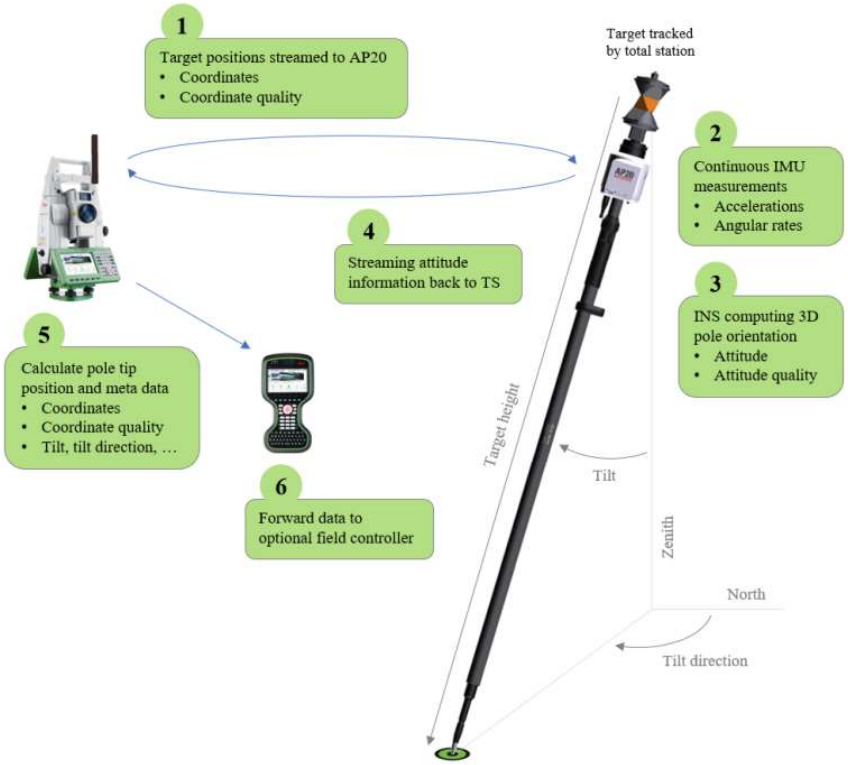

Figure 3.6: Workflow of tilt compensation with Leica AP20 AutoPole (see Maar 2022)

As figure 3.6 shows, the first step is to send a target position to the AP20 AutoPole. Therefore, the total station has to be set to lock mode (prism tracking) to follow prism's

position. The total station measures the distance respectively the angle to the (tilted) prism and stores it within a message including the coordinate quality of position. All the data is with reference to the total station's position. Via radio handle this message is send to the AP20 AutoPole (fig. 3.6: *Step 1*).
On AP20 AutoPole the IMU continuously performs acceleration and angular rate measurements. The exact measurement frequency is not communicated by the manufacturer. Nevertheless, the measurement frequency of the total station is smaller and therefore the total station is the limiting factor regarding frequency. (*Step 2*)
On the AP20 AutoPole's processing unit, the attitude w.r.t. the total station frame is calculated in *Step 3*. Therefore the algorithm needs to have the prism position in the total station's frame.
A closer view on the methological basics of tilt compensation in general is given in section 3.2.
After this calculation on AP20 AutoPole side, the attitude as well as the attitude quality are packed together into one message which is streamed back to the total station via RH18 (*Step 4*).
There, the available data is put together:

- **Target position** in the total station's frame (local or global)
- **Target height**: manual input by the user or automatic PoleHeight reading from AP20 AutoPole
- **Attitude**: pole orientation in total station frame
- **Quality data** from total station observation and AP20 AutoPole observation

The data fusion happens within Leica Captivate Field Software. The goal is to determine the pole tip coordinates of the pole as well as the points quality. (*Step 5*)
In the case of one-person operation, the final results are then streamed to the respective field controller. (*Step 6*)

For completeness, a brief overview of the data output is provided here. When examining data in *Leica Infinity*, for instance, it is evident that in addition to the already available total station observations such as horizontal and vertical angles, slope distance, and horizontal distance, additional parameters related to the AP20 AutoPole are present in the database. These include supplementary status information such as the serial number, AP20 AutoPole type, and firmware version, as well as the source of the pole height (Target Height Source) or the direction of the applied tilt compensation (Pole Tip or Opposite Direction).

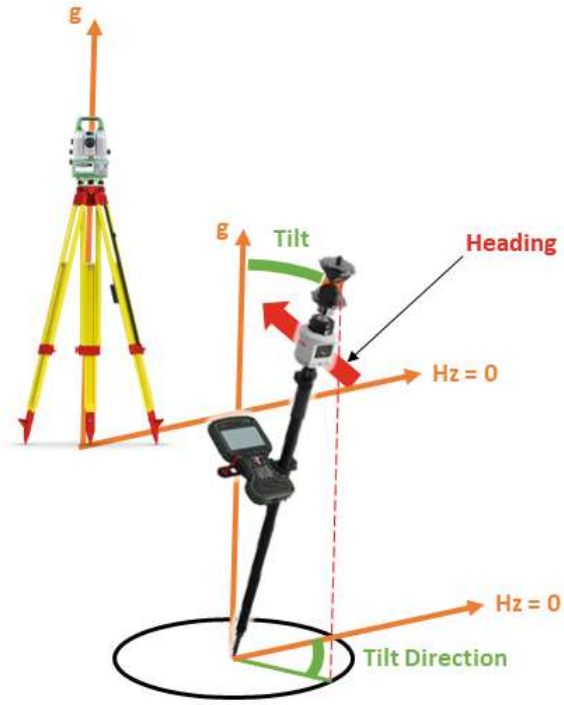

Figure 3.7: Illustration of the AP20 AutoPole output parameters

Furthermore, the observations of the AP20 AutoPole are provided, consisting of the tilt, tilt direction, and sensor heading. As illustrated in fig. 3.7, the individual parameters are defined as follows:

- **Tilt** describes the angle between the local vertical direction and the actual inclination of the pole.
- **Tilt direction** describes the angle between the horizontal zero direction and the displacement of the pole projected onto the horizontal plane.
- **Sensor Heading** is described as the rotation around the pole axis, determined by the horizontal zero direction and the sensor-defined zero direction.

From this description, it can also be inferred that for determining the pole orientation in the reference frame, only the tilt direction and the actual tilt are necessary. The tilt defines a cone with its apex at the ground point (pole tip), and the tilt direction defines the position on this conical surface. This position is therefore independent of the pole's rotation around its own axis, making the sensor heading irrelevant for defining the pole orientation.
The pole's rotation around itself becomes significant only in the case of a stakeout, where the orientation of the pole is relevant for user guidance to direct the user toward the correct direction to the stakeout point.

4. Studies

The investigations in this thesis aim to address key research questions surrounding the application of tilt-compensated measurements, specifically focusing on the AP20 AutoPole. These studies were designed to explore various aspects relevant to tilt-compensated measurements, though such aspects may not always be fully considered in practical applications. The research particularly emphasizes the practical implications of using the AP20 AutoPole. As of the time of drafting this thesis, no similar products from other manufacturers exist for comparison. Therefore, it is crucial to note that the results and interpretations derived from these investigations pertain solely to the Leica AP20 AutoPole and should not be generalized to all tilt-compensated measurement systems.
The main objectives of these studies are to provide insight into the practical application of the AP20 AutoPole, examine its impact on measurement accuracy, and assess its overall efficiency in real-world surveying tasks. The overarching aim is to answer the following key research questions regarding tilt-compensated methods:

1. **Practicality in Everyday Use**: Are tilt-compensated methods viable for daily use? Do they lead to increased efficiency, and is the accuracy level comparable to conventional surveying methods for point determination?

2. **Influence of Initialization**: What role does the initialization of the AP20 AutoPole play in point determination? Based on the investigations, which initialization movements are recommended or should be avoided?

3. **Application of Initialization Insights**: How do the findings regarding initialization affect practical surveying tasks, such as stakeout? How can the results be optimized?

These research questions were investigated primarily from the perspective of accuracy, with additional considerations given to economic efficiency and practical usability.
To ensure the scientific validity and practical relevance of the investigations, a Leica Multistation MS60 was used throughout the experiments. A detailed description of this device is provided in section 2.1. The same prism pole and field controller were used in all experiments to ensure that any equipment-related errors, such as those related to PoleHeight reading, remained constant, thus minimizing their impact on the results. Additionally, all instruments used the latest version of Leica Captivate (v8.30, latest version at the time of drafting this thesis), while the AP20 AutoPole operated on the most current firmware (FW v1.11.1.0). For data export, standard formats within Leica Captivate were employed.

The experimental studies were conducted as follows:

- An initial case study (detailed in section 4.1) examined the practical application of the AP20 AutoPole in a common surveying task: single-point capture. This study included a comparison with conventional prism pole methods, focusing on accuracy and operational efficiency.
- A subsequent investigation (section 4.2) took a closer look at the initialization process of the AP20 AutoPole, analyzing the impact of different initialization movements on the measurement results.
- Finally, the insights gained from the initialization study were applied to a practical example in section 4.3. This involved examining the effect of initialization on stakeout tasks and exploring ways to improve the outcomes through optimized initialization techniques.

These studies aim to provide scientifically interpretable results while maintaining practical relevance, offering a comprehensive understanding of the benefits and limitations of tilt compensation within the specific context of the AP20 AutoPole.

4.1. Case Study: Comparison of Pole Measurement Methods

In this investigation, the aim is to delineate the utilization as well as accuracy of the AP20 AutoPole along with tilt-compensated measurement within an artificial yet true-to-life testing milieu. Furthermore, it should be investigated to what extent the temporal (and thus subsequently economic) efficiency of the individual single-point determination methods differ.
To this end, a compact and local set of points was established (see fig. 4.1). This arrangement simulated two rectangular entities akin to parcels of land or buildings, linked via polygons representing a thoroughfare or pathway.
Reference points were delineated to facilitate the reproducible measurement of indentical points. The reference was measured using a Leica Mini Prism (*GMP111*) with a target height of 0.10m. The low target height mitigates inaccuracies in point positioning.
The stationing was conducted locally, and the station coordinates were assumed to be fixed.

$$P_{Station} = [E, N, H] \begin{bmatrix} 100 \\ 100 \\ 100 \end{bmatrix} [m] \tag{4.1}$$

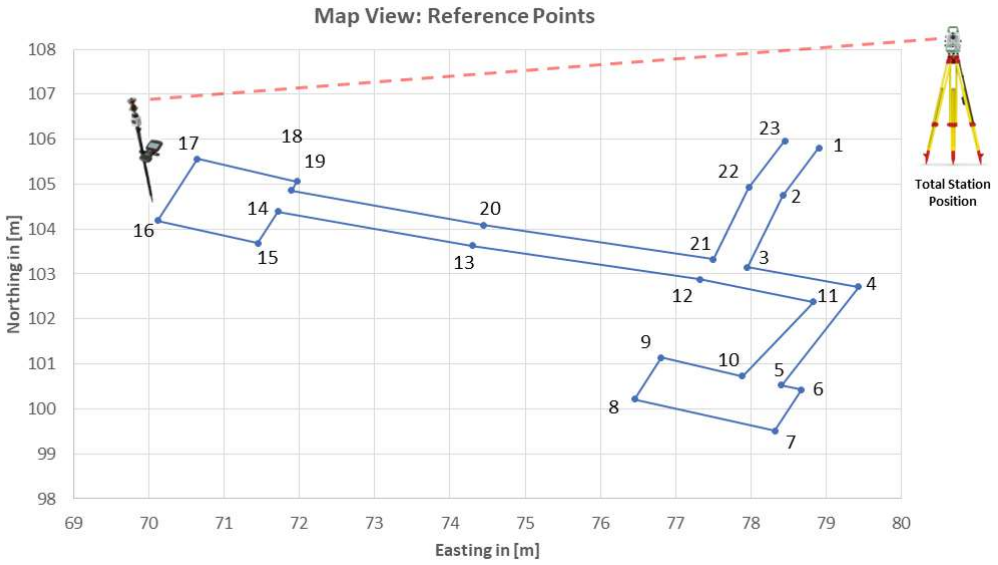

Figure 4.1: Reference point location plan

In fig. 4.1, an overview plan of the reference point network is presented. The points were measured in ascending order. Upon commencing the first measurement, a stopwatch was simultaneously started and stopped after saving the last point. When using the AP20 AutoPole, the initialization time was also included in the timing. The target height was set at 2.00m each time.
To demonstrate a comparison of different methods for determining points using a surveying pole, the following scenarios were investigated:

1. The pole is leveled by hand. Targeting was conducted in "*Lock*" mode to ensure continuous target tracking. The EDM mode was set to "*continuous*" to enable faster point storage but at a slightly lower accuracy level (w.r.t. EDM accuracy). A 360° prism (Leica *GRZ122*) was chosen, as it is the standard prism for single-operator use. It should be noted, that the prism orientation was not considered here. The influence of the prism orientation is described later in this chapter.

2. Tilt-compensated measurements by using AP20 AutoPole. Before commencing measurements, initialization was performed according to manufacturer's recommendations. The setting corresponded to those in Scenario 1.

3. The pole is leveled and stabilized with a bipod and a Leica round prism (*GPR121*) was used. Measurement is conducted as a single point measurement. The prism be sought before each measurement. Targeting is done using ATR. The EDM mode is set to "*single*".

During the evaluation process, the measured points from the different scenarios are compared with the reference point. In figure 4.2, an overview of the 2D deviation of the respective measurement points from the reference is shown.

Figure 4.2: Comparison of 2D Single Error for each scenario

The 2D single error is calculated by 4.2:

$$Error_{Single,2D} = \sqrt{\Delta E^2 + \Delta N^2} \tag{4.2}$$

It is evident for the results of this individual dataset, that the use of the AP20 AutoPole or a bipod leads to better results. Assuming a point determination accuracy of 1mm, the difference between two points results in a 1σ accuracy of approximately 1.4mm. The 2σ value, therefore, would be around 2.8mm. This rough estimation suggests that 95.4% of the differences between the reference point and the measured point would fall within a 3mm range around the expected value.

Assuming the reference point is determined with an accuracy of 1mm and the average accuracy of the points measured using the AP20 AutoPole is 12.7mm. This value is derived from the mean tilt angle of all points recorded in the experiment, adjusted according to the AP20 AutoPole datasheet specification for a target height of 2.00m. The specified accuracy, as stated in the datasheet, represents the Root Mean Square (RMS) error. Although not more precisely defined in the data sheet, a normal distribution is assumed. Based on the simple relationship in eq. 4.3, a 1σ value of 12.74 mm is obtained for the deviation of the points.

$$\sigma_\Delta = \sqrt{\sigma_{ref}^2 + \sigma_{AP20}^2} \tag{4.3}$$

By assuming a normal distribution, the 1σ value can be multiplied by 2 to calculate the 2σ

value. This results in a value of 25.48 mm. Consequently, about 95.4% of the realizations of the normally distributed random variable lie within the interval of $\pm\ 2\sigma$.
If we now examine the graphic, we can observe that 100% of the points measured with the AP20 AutoPole fall within this range.
In approximately 70% of the measurements, the points, where the pole was manually leveled using the level bubble and stabilized by hand, exhibit higher 2D positional errors compared to the points measured with stabilization or tilt compensation. In about 17% of cases, the 2D deviation is lower than in the other two scenarios. These can be considered positive outliers for the measurement result. For example Point ID 17 demonstrates submillimeter-level deviation from the reference point in the handheld measurement.
Furthermore, it is observed that points stabilized with a bipod, especially the initial points, exhibit larger 2D deviations. It can be inferred here, that there is a certain learning curve for handling the bipod at the beginning. Especially for points close to the total station, even small inaccuracies in the pole leveling lead to higher deviations for the derived coordinates on the ground.

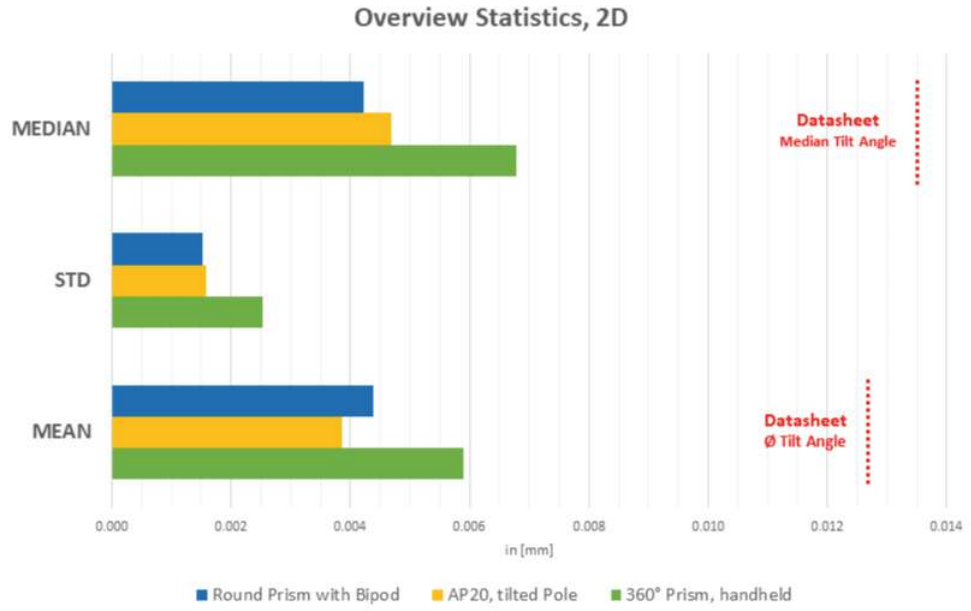

Figure 4.3: Median, Standard Deviation and Mean of 2D single error. The red dashed line shows the corresponding median and mean values, calculated by the mean and median tilt angle of the campaign. In the case study, the mean and median tilt angle were:
Mean: 12.394°
Median: 13.540°

Comparing the statistical values, it also underscores that the AP20 AutoPole achieves a similar accuracy level as the points leveled with a bipod. Further in fig. 4.3, the mean and median, specified by the datasheet ($1 \times \sigma$) and w.r.t. the mean and median angle, is

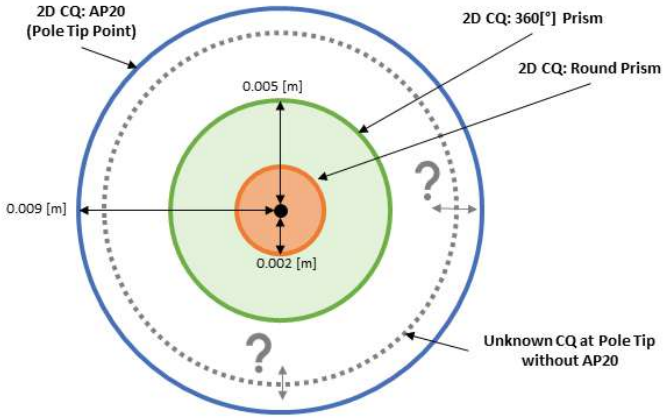

Figure 4.4: Visualization of the CQ Results within Leica Captivate for different prisms

indicated as dashed red lines. It is evident that in this specific experiment, these accuracy specifications were not exceeded. However, it should be noted that the sample size in this experiment is small, whereas the datasheet specifications are based on a much larger sample size.

Generally, for comparing the three scenarios, it is apparent that the 2D single-point accuracy compared to the reference points is worse for the handheld pole points. Both the AP20 AutoPole and the points stabilized with a bipod are generally at a similar level. Although these two methods perform at approximately the same level of accuracy in terms of deviation from the reference, when using a pole without the AP20 AutoPole, no information about measurement accuracy is provided in real-time. Consequently, users do not have immediate access to this information in the field and must retrieve it through additional steps in the data overview of the measurement job. In contrast, when using the AP20 AutoPole, real-time estimation of the current accuracy in point determination, referenced at the pole tip, is displayed.

In fig. 4.4, the graphical representation illustrates how the Coordinate Quality (CQ) results are stored in Leica Captivate. The CQ value is described as an indicator for the estimated point coordinate quality. When the AP20 AutoPole is not used, the CQ value represents the achieved accuracy of the prism measurement. Not accounted for in this value is the deviation due to a slight tilt of the pole. Therefore, this uncertainty remains unknown and cannot be reconstructed.

For better understanding, the calculation of the CQ value is detailed here:

In equations 4.4 and 4.5, the standard deviations for the angle reading and the distance measurement are provided.

Finally, using a simple error propagation, this is calculated for the 1D, 2D, and 3D cases

shown in *Leica Geosystems* (2023, p.1173 - 1174) (see equations 4.6, 4.7, 4.8).

$$\sigma_{Hz,V[rad]} = \frac{\sigma_{Hz,V[gon]}}{\rho}, \ \rho = \frac{200}{\pi} \tag{4.4}$$

$\sigma_{Hz,V}$ ... standard deviation of circle reading if$\sigma_{Hz} = \sigma_V$

$$\sigma_D = c_D + ppm \cdot D \tag{4.5}$$

σ_D ... standard deviation of distance measurement
c_D ... constant part of EDM accuracy
ppm ... ppm part of EDM accuracy
D ... slope distance

$$\text{1D CQ} = \sqrt{\sigma_D^2 \cdot \cos^2 V + \sigma_{Hz,V}^2 \cdot D^2 \cdot \sin^2 V} \tag{4.6}$$

$$\text{2D CQ} = \sqrt{\sigma_D^2 \cdot \sin^2 V + \sigma_{Hz,V}^2 \cdot D^2} \tag{4.7}$$

$$\text{3D CQ} = \sqrt{\sigma_D^2 + \sigma_{Hz,V}^2 \cdot D^2 \cdot (1 + \sin^2 V)} \tag{4.8}$$

V ... Zenith angle

However, in *Leica Geosystems* (2023, p. 1176), the CQ value is defined as a combination of the accuracy of the reflector (as described equations 4.6, 4.7, 4.8) with the attitude quality, as shown in figure 4.5.

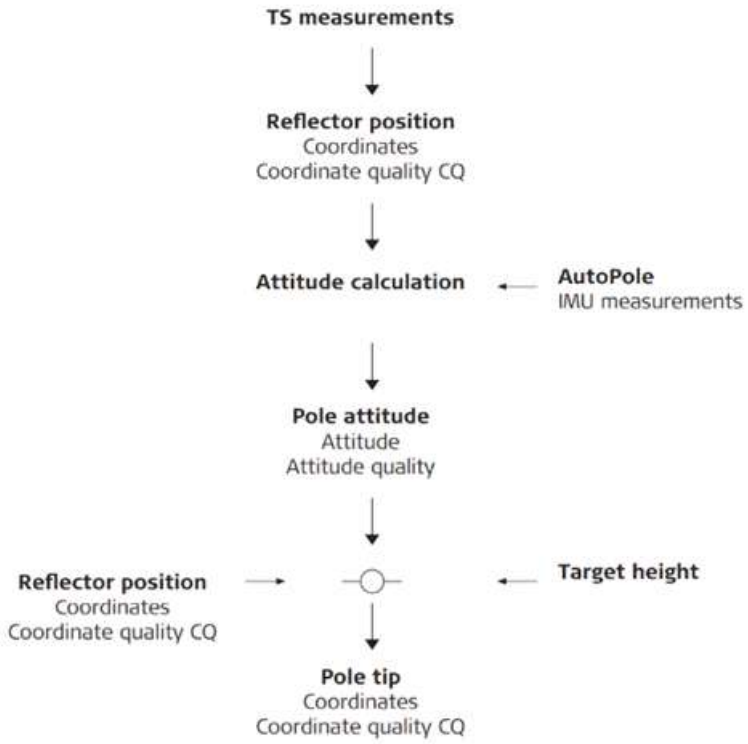

Figure 4.5: CQ estimation of TPS measurements when using AP20 AutoPole (see *Leica Geosystems* (2023, p. 1176))

Furthermore, the difference between standard deviation and the CQ value is defined in *Leica Geosystems* (2023, p. 1176), where it says:

> "The standard deviation as CQ would often be too optimistic. Therefore the computation of the CQ is not based on the basic standard deviation algorithms. There is a 39.3% statistical probability in 2D, that the computed position deviates from the true position, by less than the standard deviation. This probability is not enough for a reliable quality indicator."

It is also worth briefly discussing the use of different prism types, which were deliberately employed during the investigation. While a round prism generally offers higher accuracy, it has the significant drawback of requiring alignment with the total station. This alignment is hardly feasible and impractical in the case of prism tracking, making it unsuitable for use with the AP20 AutoPole. Any interruption in the line of sight would also disrupt the tilt compensation.
In contrast, the advantage of prisms with reflective surfaces in all directions makes them ideal for tracking applications. There is no need to align the prism, except in cases where the AP20 AutoPole is tilted within the line of sight. Here, the prism housing restricts the possible tilt angle somewhat. As shown by *Lackner* and *Lienhart* (2016),

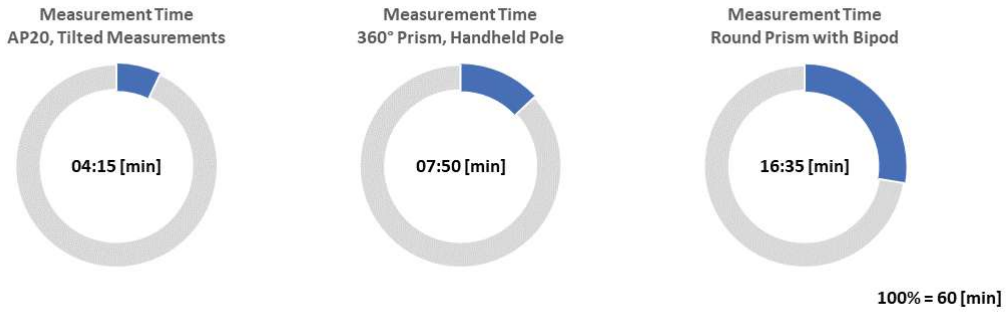

Figure 4.6: Measurement time for the different scenarios

360° prisms exhibit slightly lower accuracy compared to circular prisms. This happens due to the construction of the angled prism surfaces and can lead to minimal variations in distance measurement and angular measurement (horizontal and vertical), depending on the prism's orientation. Additionally, the author's investigations show, that for the GRZ122 prism, this variations are on a similar but low level for both tested distances (5m and 26m), which . Furthermore this publication reveals, that a GRZ122 prism suffers less variations compared to Leica's other 360° prisms.

As suplementary information, the total measurement time for each scenario was recorded (see fig. 4.6). It can be observed that the measurement time with the AP20 AutoPole corresponds to approximately 25% of the time taken for the points measured with a bipod. It should also be noted that in the timing of the AP20 AutoPole, approximately 45s - 60s of initialization time is included, resulting in the net measurement time being approximately 20% of the measurement time for the bipod measurements. The initialization time was chosen accordingly long to minimize any negative influence due to IMU initialization on measurement accuracy. A more detailed examination regarding the initialization will be provided in the next subsection 4.2).
When considering the extracted data from the AP20 AutoPole for both position and height, it becomes apparent that the actual deviations (2D Single Error) in 2D are overall smaller than those stated in the datasheet (see figure 4.7). This suggests that the specification in the datasheet are assumed more pessimistically. However, due to the small sample size of measured points, this assumption is not secure but holds true for this specific dataset.
It is also observed that the actual error (single error) varies slightly during phases where multiple points are measured within a short period and with relatively minor spatial movement. As an example, points 6 - 10 are mentioned here (see figure 4.1). This behavior may be related to a drift of the IMU during phases of minimal movement. This

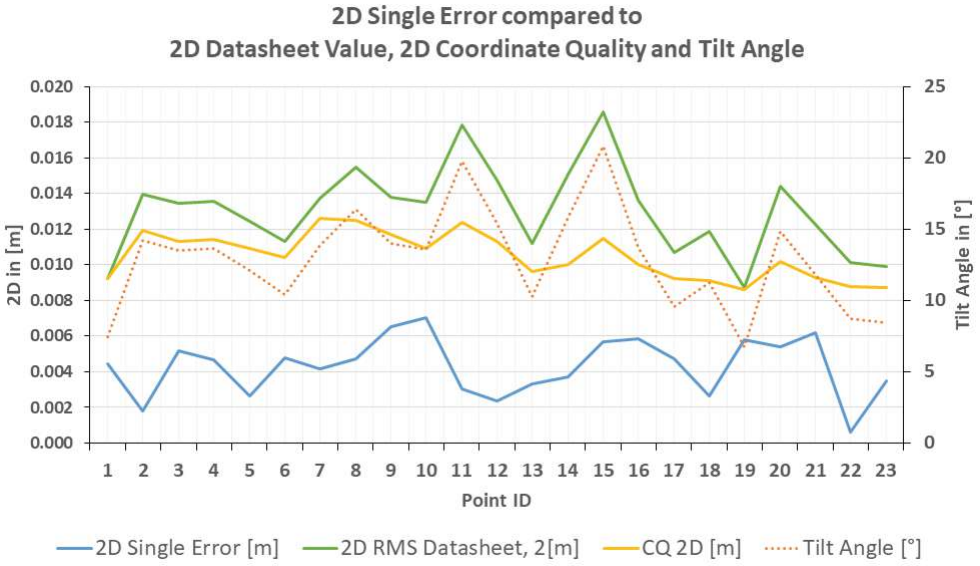

Figure 4.7: AP20 AutoPole: 2D single error compared to datasheet value, coordinate quality (CQ) and Tilt Angle

should be investigated more closely in subsequent tests (see section 4.2).

Furthermore, it is recognized that the coordinate quality (CQ), calculated by the field software (*Leica Captivate*) based on the quality of attitude and TPS observations (see subsection 3.3.4), is also more pessimistic compared to the actual observation. It is also understood that this assumption is dervied from the available dataset and therefore cannot be considered universally applicable. However, it can be assumed that in the process of specification by the manufacturer, generally more pessimistic values are assumed, and a wide range of situations are considered in this specification process.

Regarding the 1D (height) component, it is noticeable that there are instances where the datasheet specification is exceeded. Generally, it cannot be said here that the manufacturer's specification is overly optimistic. However, it is observed that, based on the dataset, the datasheet specification is neither overly optimistic nor overly pessimistic. There is also a significant deviation from the reference in Point "6". This raises suspicion that this may be a grossly incorrect measurement. Comparing the conventional methods with that of the AP20 AutoPole, it is evident that this point is generally considered an outlier (see figure 4.8). This point was poorly determined in all three scenarios. The reason for this is likely a surface with low stability. Therefore, it appears that with each placement of the pole on the surface, the underground may have yielded slightly yet not noticeable, leading to an outlier regardless of the prism used.

Similarly, comparing statistical parameters of the datasets reveals that the two variants with leveled pole are more accurate in terms of point height (see figure 4.9).The figure illustrates that both the median and mean values are lower for the leveled pole scenarios.

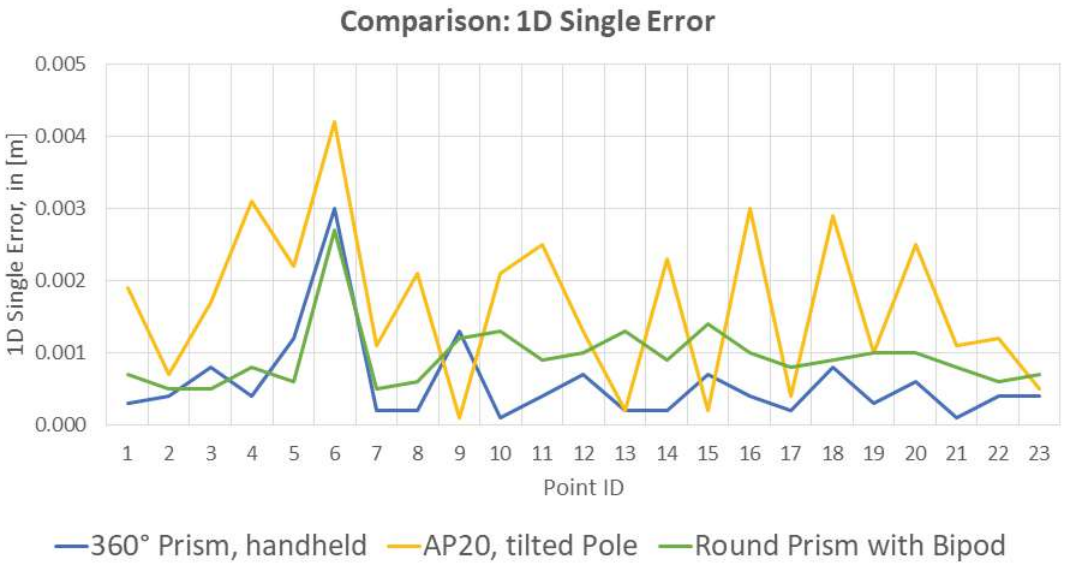

Figure 4.8: Comparison of 1D (height) single error for each scenario

Figure 4.9: Mean, Standard Deviation and Median for the 1D single error. The red dashed line shows the corresponding median and mean values, calculated by the mean and median tilt angle of the campaign. In the case study, the mean and median tilt angle were:
Mean: 12.394°
Median: 13.540°

However, the differences between the two are in the range of submillimeters, and considering measurement uncertainties, they are considered equivalent in terms of accuracy. The accuracy of height measurement here largely depends on the accuracy of the vertical angle measurement. In the case of leveled pole, any inaccuracies of the pole can be assumed to be constant and negligible, as any potential error would be equally reflected in all points. Again the mean and median, specified by the datasheet ($1 \times \sigma$) and w.r.t. the mean and median angle, is indicated as dashed red lines in fig. 4.9.
However, with a tilted pole (AP20 AutoPole), the height component is influenced not only by the accuracy of the total station but also by the accuracy of the attitude determination (IMU) and the pole itself. Depending on the tilt angle, a pole height error may be more evident in the 1D accuracy (smaller tilt angle) or in the 2D accuracy (larger tilt angle). This principle is illustrated in figure 4.10.

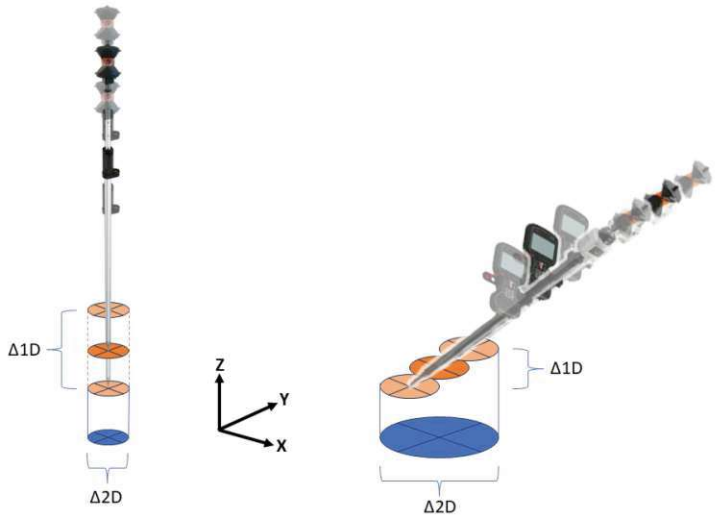

Figure 4.10: Impact of tilt angle on 2D and 1D accuracy of the ground point

In summary, it can be stated that improvements in positional accuracy result from the use of both a bipod and the AP20 AutoPole. However, employing tilt-compensated measurements with the AP20 AutoPole leads to an efficiency increase of four to five times with hardly any drawbacks in terms of accuracy. It is worth noting that the selected points correspond to a small-scale area.
Furthermore, an advantage of the AP20 AutoPole is the real-time display of coordinate quality within field software, providing the user with direct feedback on the current accuracy. Thus, the user can intervene in case of poor estimated quality, for example by saving the point only after further movements to increase the attitude quality (visible in the "Quality Bar" in the upper area of the user interface).
In conclusion, it can be recommended to use a lower target height to increase accuracy, provided that a higher level of accuracy is required and this is feasible due to the local

conditions. As an example, reference can also be made to the manufacturer's specifications for the use of the so-called "reverse mode", where the pole is used upside-down and the target height decreases to 0.228 m, specifying the following accuracies:

- 2D: 1 mm + 0.1 mm/° Tilt
- 1D: 1 mm + 0.05 mm/° Tilt

The results of this investigation met the manufacturer's specifications, but due to the small sample size, they are not suitable for providing a definitve confirmation of the claims Leica states in the datasheet. A comprehensive verification would need to be conducted, considering a much wider range of tilt angles as well as different distances to the target. However, since this investigations is a case study based on typical everyday use, it can still be considered representative, and the results can be used to adress the research question.

4.2. Analysis on Initialization and Influence on Tilt-Compensated Measurements

As mentioned in the first test (see subsection 4.1), a prolonged initialiazation phase with various arbitrary movements was chosen before the measurements. On one hand, this is recommended by the manufacturer, and on the other hand, it is visualized in the fild software *Leica Captivate*, providing the user with direct feedback on the quality of attitude in real time.
In the research question regarding initialization mentioned at the beginning of this section, the following focuses of this study now arise:

1. Does the duration of the initialization phase affect the quality and duration of the tilt compensation after initialization?
2. What effect do different initialization movements have, and can a specific type of movement be recommended?

In a first test, the stability of the position measurement of the AP20 AutoPole over an extended period was examined when the pole was static after initialization. Furthermore, it was intended to demonstrate how the duration of initialization affects an immediately following static phase.
For this purpose, different initialization intervals were defined. Subsequently, the pole was statically positioned stabilized using a bipod.
The interval durations were:

$$\begin{bmatrix} 3 \\ 10 \\ 20 \\ 60 \end{bmatrix} [s]$$

In this context, a stable phase refers to a phase in which points could be measured in the field software. Since exceeding a defined threshold deactivates the tilt compensation, saving a point is only possible after reinitialization. The threshold refers to the attitude quality, which is determined by the quaternion quality on the side of the AP20 AutoPole according to the manufacturer.
Subsequently, points were measured using the *Leica Captivate* internal function "Auto-Points", with the highest possbile recording frequency selected, which is 10 Hz. The point measurement is performed in AutoPoints with the first possible point after falling below the attitude threshold and ends with the last possible point that is below the threshold. The timing of the initialization and the ongoing static phase until reaching the threshold were measured using a stopwatch.
During the initialization phase, motion patterns were arbitrarily combined, following recommendations of Leica Geosystems [2]:

- Move the pole (while walking or being static) in different directions
- Do not move the pole too fast or too slow
- Continue the movement after the initialization "beep" (of AP20 AutoPole) for a minimum of 5s

This results in motion patterns, which were randomly combined with different speeds and different number of repetitions and performed during a walking movement. The results are presented below, starting with the respective time span in fig. 4.11 until the threshold was reached while the pole was stable.

[2]https://www.youtube.com/watch?v=KL995DZEe3c

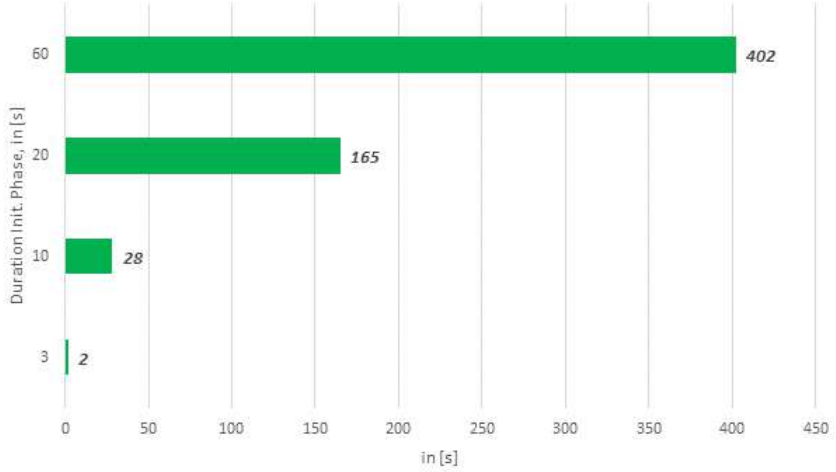

Figure 4.11: Timespan while point storage is available when pole is stable after different durations of initialization

The results confirm, on the one hand, what is prescribed by the manufacturer, and they also support the assumption that by extending the movement duration for initialization, both the bias and drift can be better estimated, thereby improving the attitude determination even during periods of little movement.
When comparing the two plots in fig. 4.12 and 4.13, it is evident that the drift behaviour after a longer initialization phase is approximately linear throughout the entire drift phase. In contrast, with an initialization phase that is one-third short, two independent linear phases emerge, interrupted by a shorter but distinct opposing drift motion.
Examining the static phase of the pole in terms of Euler angles, however, reveals a drift behaviour over time, particularly in the Yaw angle which can be seen in fig. 4.12. The drift of Yaw also correlates strongly with a drift in the Roll, which corresponds to the rotation along the pole axis and, according to the manufacturer, does not affect the calculation of the pole tip coordinates. Therefore, this drift is neglected hereafter. Due to a small tilt angle during the static phase, this drift in the Roll may arise from a cross-coupling effect, described in section 2.2.3.2. However, a sensor drift cannot be ruled out, as no further investigations in this regard were conducted in the course of this thesis. Conversely the Pitch angle is considered stable. This corresponds to the tilt angle of the pole, which is the angle between the local gravity vector and the actual inclination of the pole.
The same behaviour can also be observed for the 20[s] initialization, although in this case, the correlation between Roll and Yaw is less pronounced (see fig. 4.13).
The results are only presented for the initialization durations of 20s and 60s, with further results available in the appendix.
Figure 4.12 depicts the change relative to the first measurement of the static phase.
An explanation regarding the Yaw drift will be provided later in this chapter.

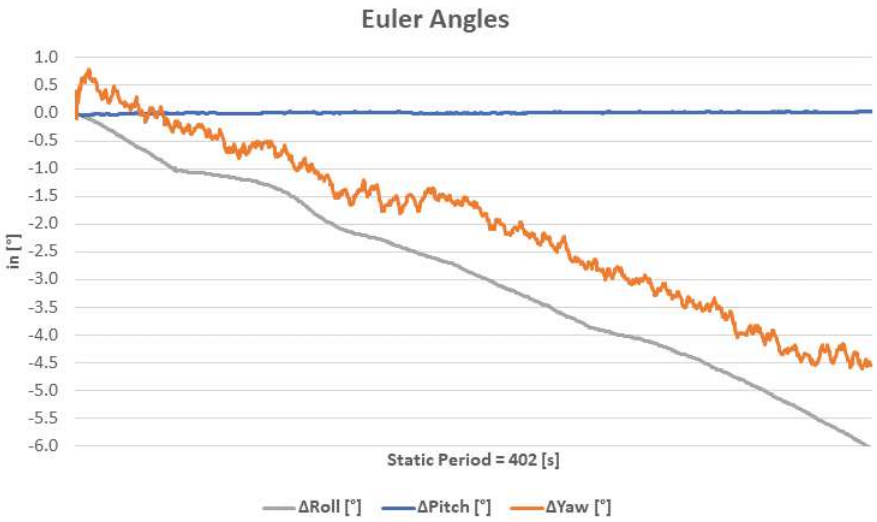

Figure 4.12: 60s Initialization: Timespan after initialization phase until tilt compensation is stoppend. The pole is stabilized.

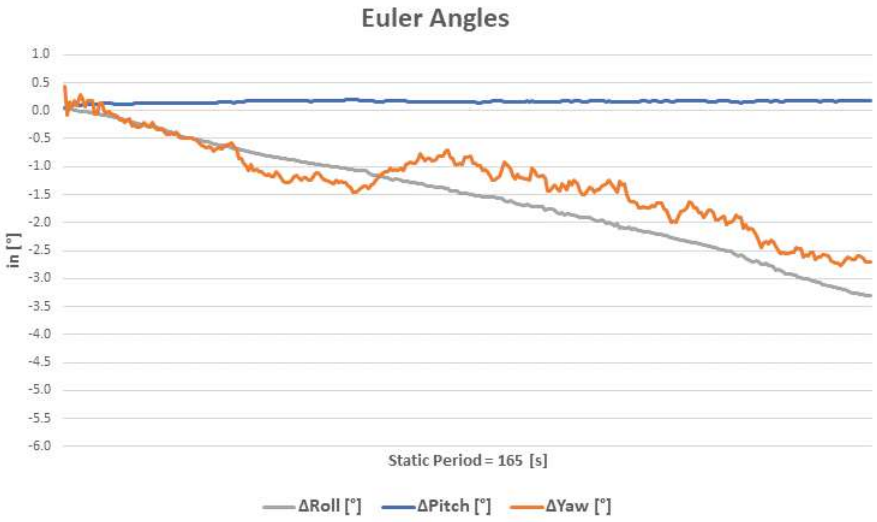

Figure 4.13: 20s Initialization: Timespan after initialization phase until tilt compensation is stoppend. The pole is stabilized.

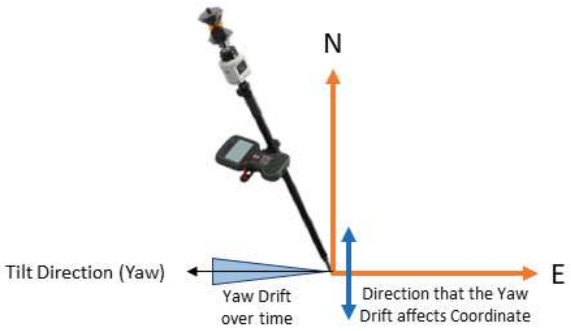

Figure 4.14: Principle how the Yaw drift affects a coordinate: the blue triangle symbolizes the drift (=slow movement counter-/clockwise) from the actual tilt direction (black arrow). The blue double arrow shows the affected direction of the coordinates

Subsequently, the impact on the coordinates is also illustrated here (see fig. 4.15 and fig. 4.16). It can be observed that the drift of the Yaw angle particularly affects the North component. This can be explained by the station orientation. The inclination occurs perpendicular to the North direction, causing a drift of Yaw in this same North direction. The principle is shown in fig. 4.14

The impact of the drift on the pole tip coordinates is therefore also dependent on the definition of the coordinate frame. Based on the assumptions before, the least impact would occur if the pole were inclined 45° between the axes, as this would evenly distribute the drift across both coordinate axes. However, this assumption is hardly practical in everyday use.

In the coordinate plots (see fig. 4.15 and fig. 4.16), it is evident that there is still a slight influence on the Easting component, whether minimal. This can be attributed to the imprecision in determining the tilt direction (=Yaw). Consequently, slight drifts in the Easting component occur.

However, the Height component remains virtually stable throughout the static phase. This is because it is primarily dependent on Pitch, and this angle remains very stable over the duration of the static phase.

Based on these findings, an initialization time of 60s was set for the subsequent initialization investigations. This time was measured with a stopwatch. Furthermore, initialization movements were defined, as depicted in figure 4.17.

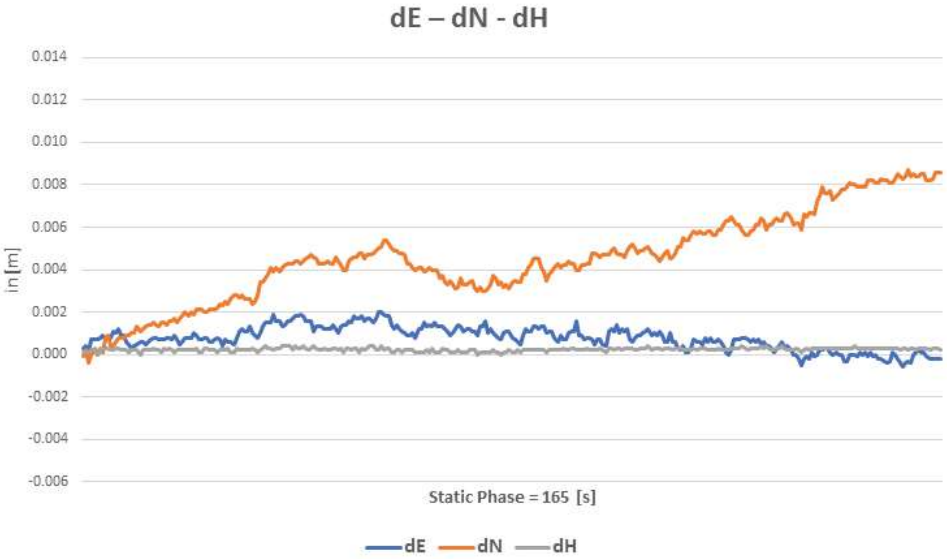

Figure 4.15: 20s Initialization: Drift of ENH coordinates over time during static phase with reference to the first point of static phase.

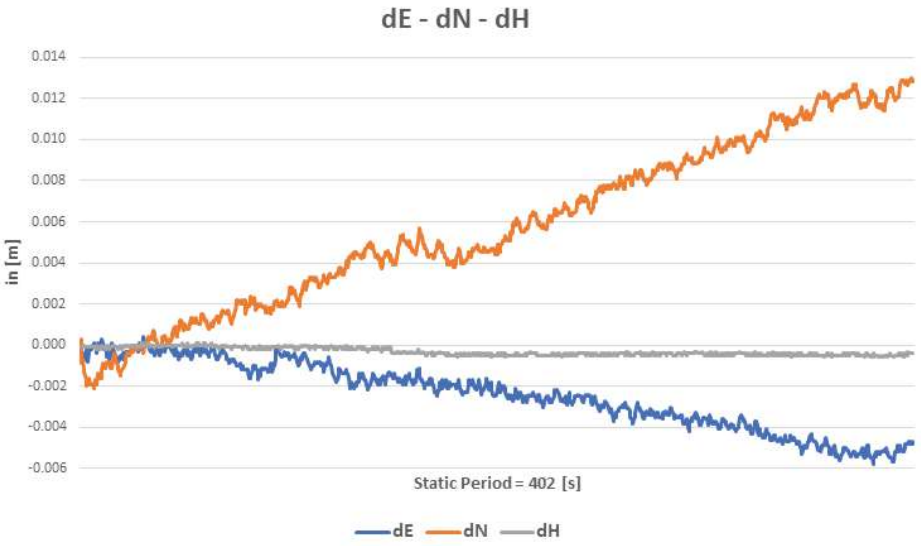

Figure 4.16: 60s Initialization: Drift of ENH coordinates over time during static phase with reference to the first point of static phase.

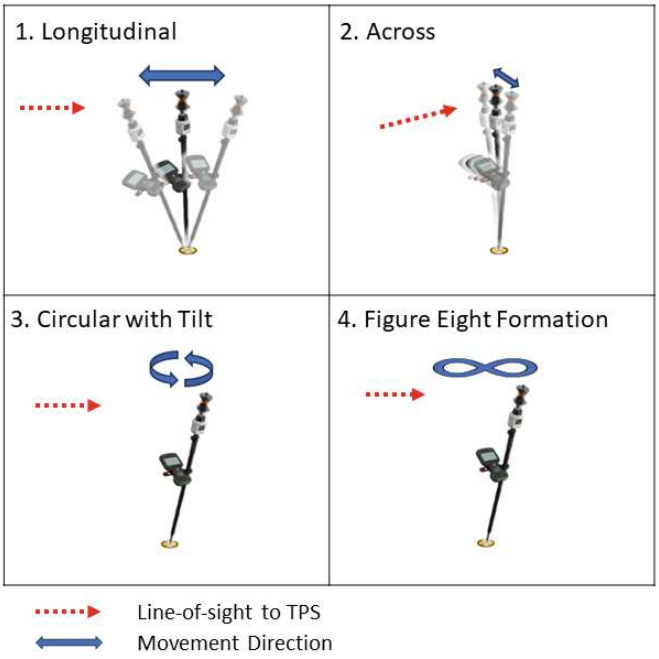

Figure 4.17: Performed movement patterns

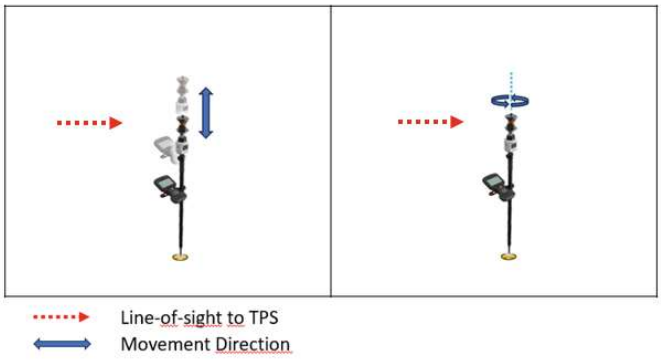

Figure 4.18: Movement patterns with failed initialization

Additionally, a combination of all these variants was performed.
Throughout all tests, the orientation of the AP20 AutoPole remained constant in the direction of the total station to avoid influences due to rotations around the pole axis.
The movements were performed slowly and then fastly. It should be noted here that the fast movement is hardly practical, as it does not correspond to a natural, intuitive movement speed. Nevertheless, the two different speeds were used to investigate whether there is an influence of movement speed and, if so, to what extent it affects faster convergence behavior.
Additionally, an up-down movement was performed. However, the initialization was not successful with the movements depicted in figure 4.18. This is because in a pure up-down movement, there are no accelerations and rotations in the x-y plane (horizontal plane),

and thus the bias-drift components of the filter cannot be sufficiently determined. A more detailed explanation will be provided in the later analysis of the other successful movement patterns. Consequently, this leads to inadequate convergence of the IMU, so the system's internal threshold is not reached. Therefore, the AP20 AutoPole cannot provide measurement data as it is recognized by the system as too inaccurate and uncertain.
The same happens with a fast rotation around the pole axis. Additionally, the lack of acceleration in the z-axis limits the value in this axis to the gravitational acceleration. This creates an unfavorable situation where there is rotation around the z-axis, but the acceleration value hardly changes. This also leads to poor bias and drift estimation.
These two types of movements were subsequently disregarded and not further investigated. Since initialization of the AP20 AutoPole was not possible, no data could be recorded, and therefore no evaluation is possible. Furthermore it should be noted here, that the terms $Q_{xx,yy,zz}$ refers to the standard deviation of the quaternion attitude.

All the successful experiments were conducted with a tilt angle of approximately 15°-20°. This inclination corresponds to a normal deflection within the range of motion of an user's arms.
After a 60-second initialization phase, the pole was stabilized in a vertical position with a bipod. After interrupting the continuous measurement due to the threshold of the attitude quality parameter being exceeded, the measurement was stopped.
For the static phase, a vertical position was chosen based on the results from section 4.2 to minimize correlations between the individual components. All measurements were conducted, as in the previous investigations, with a target height of 2.00m.
In all figures shown here, the red dashed line symbolizes the start of the static phase. To improve readability, the scale of the horizontal axis was replaced by the total time, which includes both the initialization phase and the subsequent static phase. In the graphs, it can be observed that there is already a slight drift phase before the start of the static phase. This is because fixing the pole to the bipod in a vertical position takes a small amount of time. This phase is already quasi-static, with little movement and only slight corrections, resulting in a slight drift beginning.
The horizontal axes were scaled to improve comparability. From now on, the plots show the quaternion quality and not Euler angles anymore. The reason is, that the Euler angles cannot display the influence of initialization movements during the initialization phase and how they affect the whole process.

At the beginning, the results of the linear movements (longitudinal, across) will be discussed.

In these two executions (see fig. 4.19 and fig. 4.20), the difference between a fast and slow

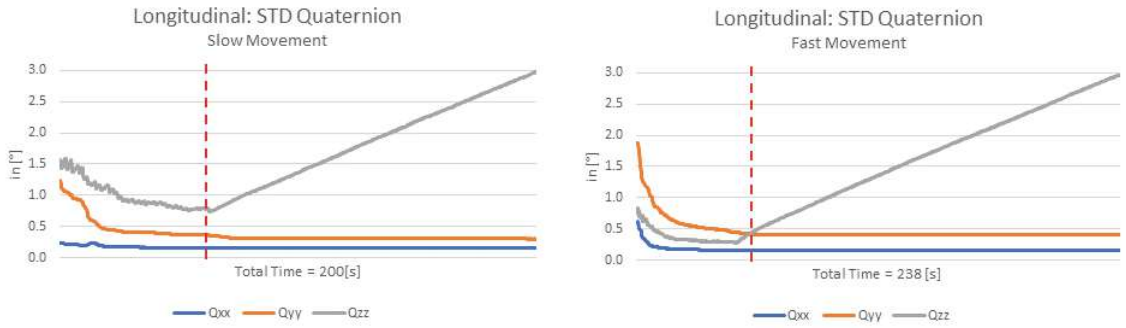

Figure 4.19: Initialization: longitudinal movement

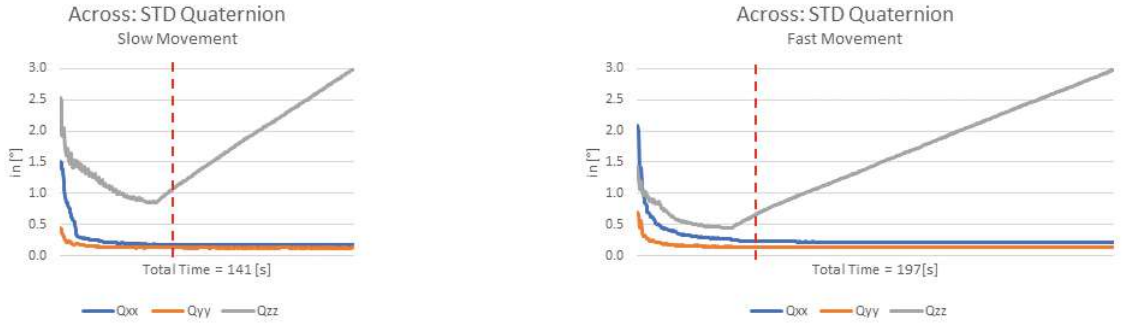

Figure 4.20: Initialization: across movement

movement is clearly evident. While the slow initialization movement, both longitudinal and across, shows a rather slow convergence behavior, it can be seen that a fast movement positively influences the estimation of the IMU error parameters. When considering the total times, there is a significant difference, especially in the across movement. They are approximately 25% shorter compared to the longitudinal initialization. One possible reason for this is that in the longitudinal movement, distance changes are also present and therefore taken into account in the Kalman Filter, whereas in the across movement, there are hardly any distance changes, and besides the IMU data the observations mainly rely on changes in angles, primarily the horizontal angle. The combination of unidirectional accelerations, along with the minimal change in distances and consequently the consistently imprecise and barely changing distance measurements, likely leads to a delayed and difficult improvement of the filter solution. This weak filter can subsequently result in faster drift during static conditions.

Furthermore, it can be observed that the parameters Q_{xx} for longitudinal movement and Q_{yy} for movement perpendicular to the line of sight are well determinable from the beginning and therefore have a relatively low standard deviation. Subsequently, these parameters hardly convert anymore.

In general, it can also be observed that these parameters do not undergo significant drift.

They obviously converge to a saturation level and remain there, even in the static phase. These observations are also made in studies by *Teodori* (2019).
However, the trend of the standard deviation of the z-component Q_{zz} is particularly notable. This can be observed to the same extent in all movement patterns (see fig. 4.21, fig. 4.22, fig. 4.23). This drift occurs as soon as a static or quasi-static phase takes place. *Groves* (2013, p.575) explains this by stating that the observability of the yaw error state is only achieved through horizontal accelerations. *Teodori* (2019) also confirms in his simulation studies that accelerations in the horizontal plane lead to a positive change in the standard deviation. It should be noted that in Teodori's studies, investigations were conducted at the level of Euler angles, whereas in this work, the attitude standard deviation is considered based on quaternion results. However, this statement can also be illustrated in the initial tests conducted at the beginning of this work (see fig. 4.24). In the figure, it can be observed that immediately after the tilt compensation was stopped by the field software, a simple movement in the horizontal plane leads to a rapid reinitialization, and the standard deviation quickly decreases to a low level again.

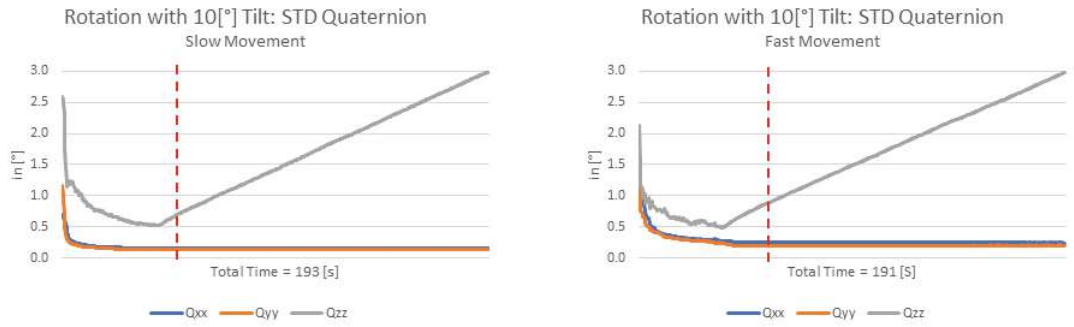

Figure 4.21: Initialization: rotation with tilted Pole (Tilt = 10[°])

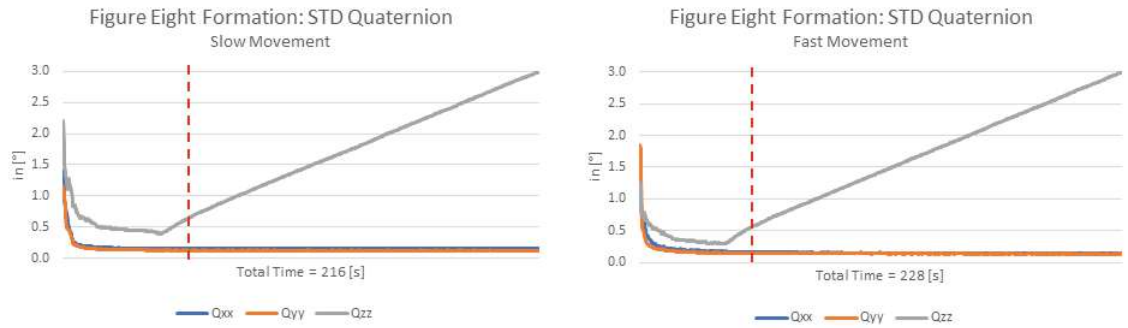

Figure 4.22: Initialization: figure eight formation

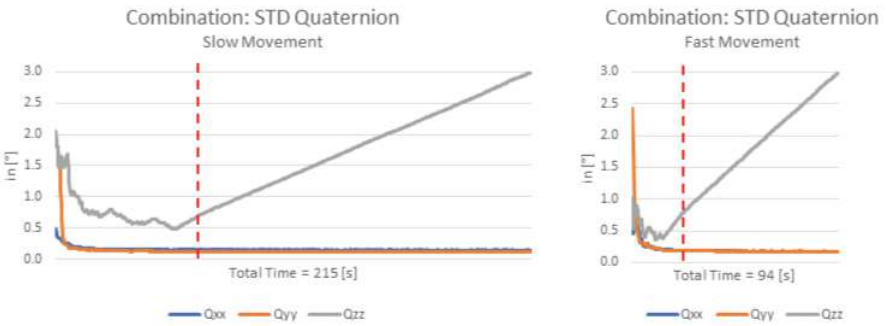

Figure 4.23: Initialization: combination of all performed movements

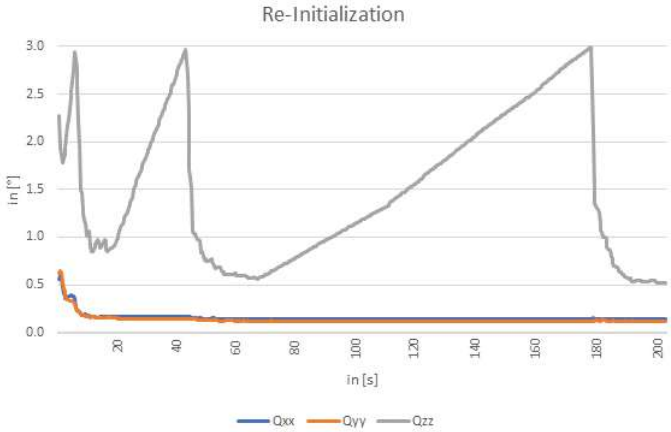

Figure 4.24: Standard deviation behaviour after reinitialization

During static phases, the drift strongly depends on the propagation of the IMU accuracy. This also explains the similar trend in the static phase in all different initialization movements. Consequently, the differences in the total times can be explained as well. This time ultimately depends on the value of the standard deviation before the static phase. The manufacturer's defined threshold of the standard deviation of 3° determines how quickly or slowly this is reached, depending on the initial standard deviation's level. But this does not apply to the fast movement with a combination of all movement patterns (see fig. 4.23). It is clearly noticeable that in this combination, the convergence phases are repeatedly interrupted by phases with little convergence or even divergence. These effects are likely due to the frequent, short-term changes in direction when combining the movement patterns. As a result, the total station may not immediately follow them because the prediction of target tracking requires a brief moment for direction correction. Due to the low measurement rate of the total station or the very high measurement frequency of the IMU, this leads to a temporary, distorted attitude determination. Nevertheless, this does not result in gross errors, as they can be controlled through the estimation of the

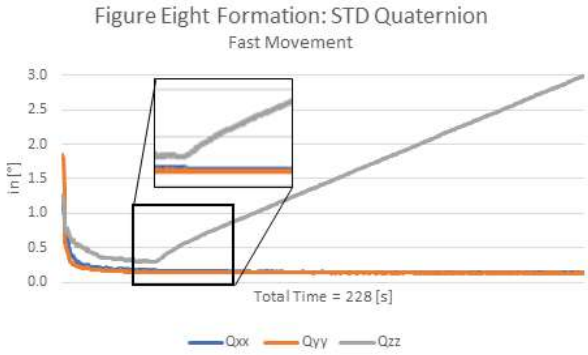

Figure 4.25: Stronger increase in the standard deviation shortly after transitioning to a (quasi-)static phase.

Kalman filter. In the subsequent section, this effect will be depicted more precisely in the graph.

It should be noted that this effect must be considered as temporally local and of low magnitude. Therefore, there is no noticeable impact on the user. With a slow initialization, these divergence phases are noticeably reduced, and in a global view of the trend, convergence of the standard deviation can be observed.

Taking a closer look at those movement patterns that exhibit accelerations in all directions in the horizontal plane (see fig. 4.21 and fig. 4.22), it is evident that besides a fast, strong convergence of the standard deviation of the x- and y-components, even in slow movements, the standard deviation of the z-axis already decreases to a lower level (0.4° – 0.5°). Compared to the linear movements in fig. 4.19 and fig. 4.20, this corresponds to a halving of the standard deviation. However, no difference is seen in this regard with fast movements.

Furthermore, it is noticeable here that especially shortly after the start of a quasi-static phase (small movements to fix the pole using the bipod), there is a temporary, stronger increase in the standard deviation of the z-component. This is magnified in fig. 4.25 and applies especially to the movement patterns shown in fig. 4.21 and fig.4.22. This suggests that due to the lack of horizontal accelerations in this phase, the IMU accuracy has a stronger influence on the error state estimation. Additionally, a contribution from the spontaneous, abrupt transition from a movement phase to a quasi-static or static phase cannot be ruled out, as it temporarily leads to an increase in the innovation of the Kalman filter due to the difference between prediction and actual observation. Consequently, the covariance of the innovation also temporarily increases. Since no further system data are available for this study, this assumption cannot be further confirmed.

All the results presented so far, as shown, relate to a natural pole deflection of approximately 15° - 20° tilt.

In another initialization test, the hypothesis to be investigated was whether a larger tilt angle would lead to an improved determination of the unknown parameters drift and bias. This improved determination should subsequently be reflected in faster convergence of the quaternion quality parameters.

In this test, the same movement patterns were performed as in the investigation with less tilt. The only exception was the movement in the line of sight, as there is an interruption in the line of sight due to the shape of the 360° prism, resulting in a break in the tilt compensation. Similarly, the movements classified as failed in the previous test (fig. 4.18) were neglected.

The initialization was performed at a moderate pace since previous experiments have shown that fast pole movement does not necessarily lead to faster convergence in all the movement patterns. Furthermore, it has been explained that the drift rate in the static phase mainly depends on the accuracy propagation of the IMU and not on the movement pattern. Only in linear movements, it was shown that there is an influence of speed. However, for the sake of comparability between different movement patterns, a moderate, practical speed was chosen.

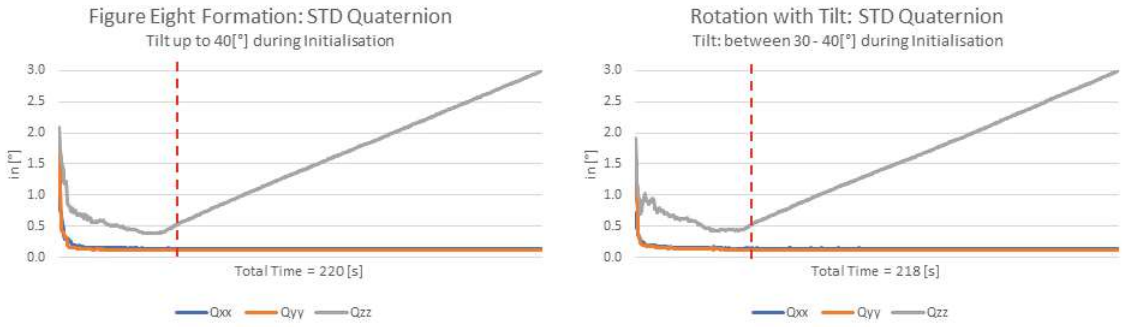

Figure 4.26: Initialization: figure eight formation (left) and rotation with tilt (right)

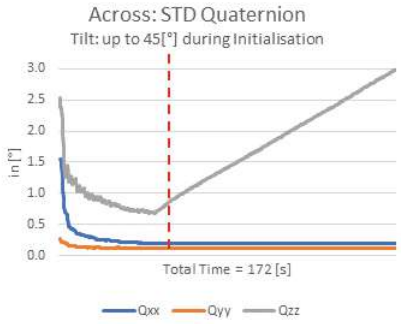

Figure 4.27: Initialization: Across movement with a tilt angle up to 45[°] (horizontal axis is scaled w.r.t. fig. 4.26)

Comparing the results here to those from the previous investigations with a smaller tilt

angle, hardly noticeable differences can be observed (see fig. 4.26). In the circular movement with the tilted pole, slight variations in the convergence phase are visible, especially at the beginning. One possible reason for this is the human factor. Since the rotational movement was not automated, there is a deviation from the ideal circular motion in the vicinity of the human body due to the large tilt angle. Here, the circular motion approaches an elliptical path, and it tends to resemble linear motion when facing the body (similar to the across movement pattern). This movement can introduce some uncertainty into the error state estimation in the initial phase. Although efforts were made to follow the circular trajectory as closely as possible in this area, complete avoidance of deviation is not possible.

A similar pattern is also seen in fig. 4.27 at the beginning of the across movement. Similarly, the tilt angle in the line-of-sight of the total station could not be maintained at 40° because there is already a line of sight interruption and subsequent loss of lock due to prism tilt.

Based on these results, the influence of larger tilt angles on potential faster convergence or smaller standard deviation cannot be confirmed. It appears that the saturation level is similar to that of the experiments with smaller tilt angles.

In the combination of all movement forms (across, rotation, figure eight), it was observed that during the initialization phase, there were two peaks. In fig. 4.28, these peaks are compared to the movements during initialization, represented by the measured tilt angle. It can be seen that shortly before each peak, a brief static phase occurs. This phase is limited to a maximum of 2s - 3s during the execution of the initialization. Looking at the subsequent significant change in tilt angle from 35° - 40°, this abrupt increase can be attributed to poor attitude estimation and the resulting poor covariance of attitude estimation. What is noticeable, however, is that when a movement in different directions (i.e. rotation with tilt) occurs immediately after the rapid change in tilt angle, the standard deviation recovers faster and even drops below the level before the brief static phase. In comparison, it takes longer in terms of time for the standard deviation to return to at least the level before the peak in a linear direction, where accelerations mainly occur in one axis. It can be concluded that large changes in tilt within a short time after a static phase are problematic for the accuracy of attitude determination. Since the AP20 AutoPole communicates this information to the total station, significant deviations in point determination are expected during this short phase. This should be considered in the application of the AP20 AutoPole, especially if a short quasi-static phase occurs during which, for example, an input is made on the field controller, followed by a very rapid execution of a high tilt angle.

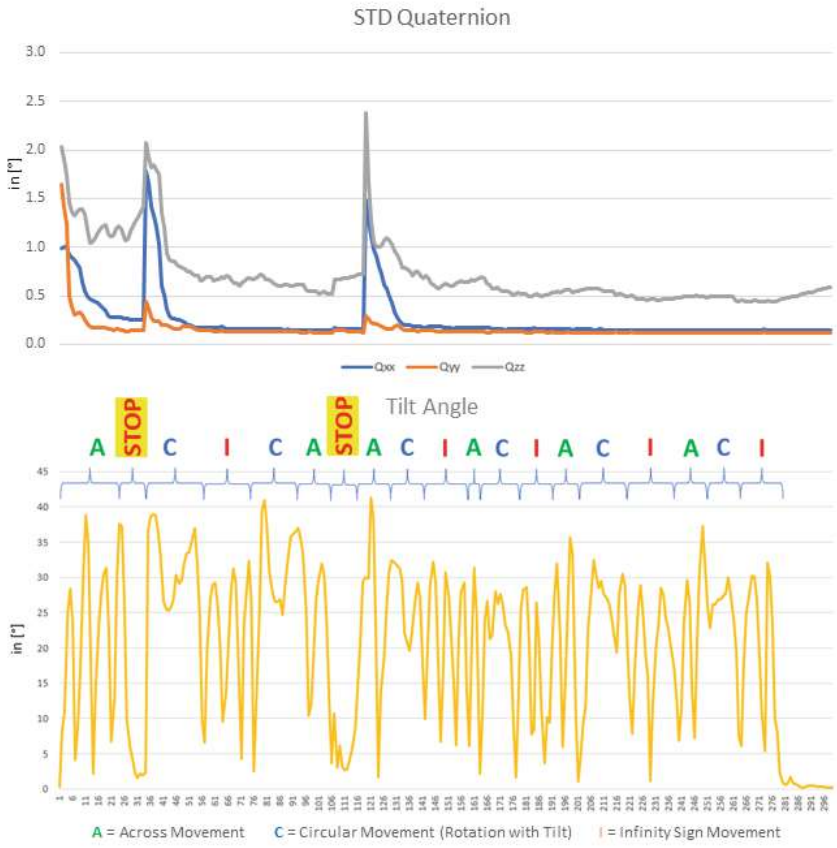

Figure 4.28: Comparison of movement patterns and the corresponding effect on the attitude's standard deviation

In summary, the conducted investigations have shown that when using the AP20 AutoPole for successful and long-lasting tilt compensation, both the duration of the initialization phase and the type of movement performed are crucial factors. Especially in cases where little movement occurs in the survey area after the initialization phase, an initialization duration of around 60s is recommended.

From the examined movement patterns, a clear recommendation also emerges for movements that cover as many directions in the horizontal plane as possible. Specifically, a figure eight formation proved to be very advantageous in the investigations, as it ensured fast convergence and achieved a lower saturation level in terms of standard deviation.

It was also demonstrated that after short static phases, a high tilt angle can be problematic in terms of achievable point accuracy. Therefore, it is recommended to avoid large tilt angles even after short static phases, or to perform a short movement in different directions immediately after a static phase to avoid gross errors in the measured point.

These findings will be applied in a further investigation to a practical surveying task.

4.3. Effects of the Initialization Quality on Stake Out

This experiment aims to apply the insights gained so far to an everyday surveying task from practice: stakeout.
A major advantage of tilt-compensated measurements during stakeout is that it allows more focus on the point to be staked out, for example, through visual guidance in the field software. However, as seen in previous experiments, this also brings some challenges. Typically, as one approaches the point to be staked out, movements become smaller. This is not a problem in the conventional method with a prism pole that is brought into a vertical position using a level bubble. However, in the application of the AP20 AutoPole, previous investigations have shown that due to the lack of movement in quasi-static phases, there is a continuous deterioration in attitude quality and thus in the final point estimation.
The following experiment aims to demonstrate this effect and ultimately show how the problem can be overcome.

The experimental setup is as follows:
The quasi-static phases are simulated by positions that are at defined distances from the actual stakeout point, with the distances between these quasi-static points decreasing towards the stakeout point. This simulates navigation towards the selected stakeout point. Usually, during this navigation, the movement decreases as one gets closer to the selected point. For this purpose, points were defined at specified intervals from the stakeout point and coordinatively determined. These points simulate the mentioned navigation movement and represent a short static phase of about 5s, during which the user, for example, looks at the field controller. During these 5s, the pole was manually held static and an almost vertical position was ensured. Figure 4.30 schematically depicts the setup. The reference point coordinates were overdetermined in advance by measuring with a mini prism and were established by simple averaging (see fig. 4.29).

	Easting [m]	Northing [m]	Height [m]	Interval to Stake Out Pt. [m]
Stake Out Point	*97.522*	*112.604*	*97.964*	*0.000*
D-0.04	*97.511*	*112.645*	*97.964*	*0.042*
D-0.08	*97.500*	*112.682*	*97.964*	*0.081*
D-0.15	*97.483*	*112.749*	*97.963*	*0.150*
D-0.30	*97.441*	*112.891*	*97.963*	*0.298*
D-0.50	*97.380*	*113.084*	*97.963*	*0.500*

Figure 4.29: Coordinates of Reference Points

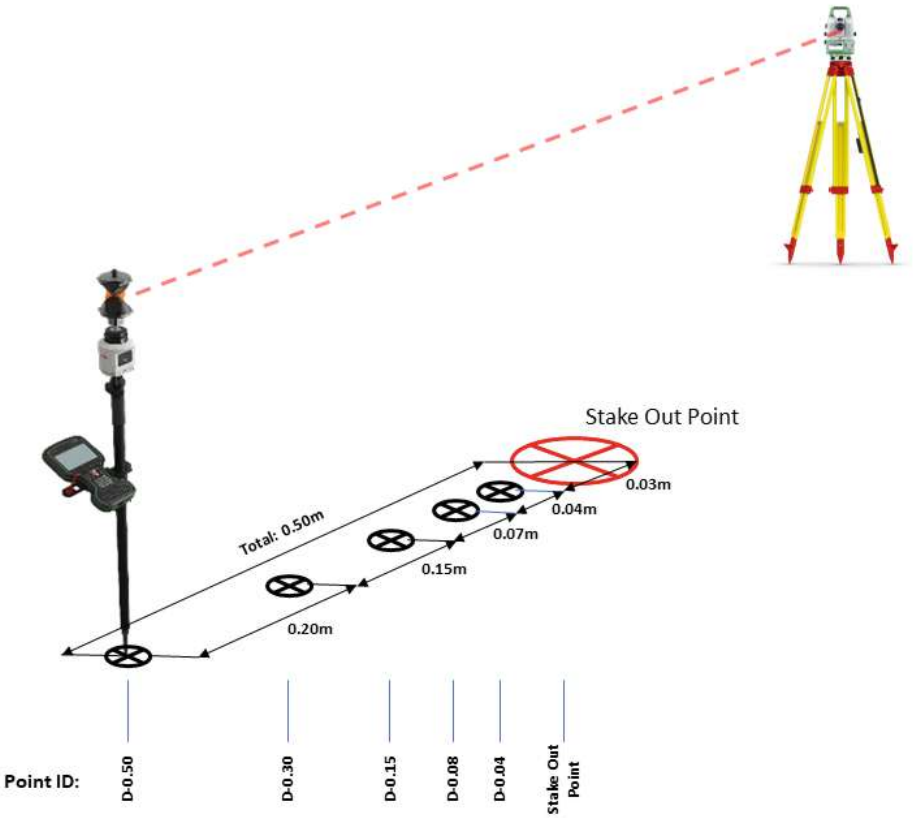

Figure 4.30: Stake Out: Measurement Setup

Before the measurements, a 60s initialization phase with an figure eight formation was conducted according to the results from Section 4.2. Following the initialization phase, the measurement of individual points towards the stakeout point commenced immediately.
It can be observed that in the initial phases where the point distances are higher (points *D-050, D-0.30, D-0.15*), the 2D position error continuously decreases. This is mainly due to the movement of the AP20 AutoPole in the horizontal plane, as discussed in section 4.2, which subsequently has a positive effect on the standard deviation of the attitude determination. However, as the movements decrease towards the stakeout point, the lack of motion is reflected in the point position error. There is a sudden increase at point *D-0.08*, where the motion from point to point decreases. Here, a certain plateau is reached, where the 2D error stays at between 6 - 7 mm. In contrast, no pattern can be observed with a shorter initialization time. The results for individual points vary randomly within a range of 5 to 8 mm, and the final stake-out point was not reached due to an interruption in tilt compensation. Although the difference in 2D error between 10s and 60s initialization times is only about 2mm, it can still be demonstrated that good initialization combined with a subsequent sufficient movement phase (e.g. towards the stake-out point) has a positive effect. This positive effect is evident as there is no significant increase in error

during phases with greater movement. In this specific case, there is even a reduction in the 2D error. The 2D error only worsens when the movement phases become shorter, resulting in fewer accelerations due to the movement (see fig. 4.31 and fig. 4.32). At the final stakeout point, a 2D deviation of approximately 7mm from the previously measured reference is reached for the 60s initialization phase.
Looking at the CQ value, it can be seen that it ranges between 8.1mm and 8.3mm for all points. By the definition of CQ given in section 4.1, and based on the current configuration and the data available to the algorithm, this seems to be the minimum achievable value for this pole height and the chosen prism. Based on the data, it could be inferred that the CQ value is reported pessimistically compared to the datasheet specification. But again, this conclusion cannot be definitively drawn here because the specification was derived from a large number of points recorded under various conditions, according to information from the manufacturer. To verfiy this, further investigations would be needed, including a larger quantity of points.
Depending on the task and the required tolerance, a 7mm deviation may already exceed the specified tolerance. Typical tolerances range from a few millimeters in steel construction to a few centimeters in building construction. For cadastral surveys, where the stakeout accuracy is in the mid-single-digit centimeter range, the accuracy is sufficient.
To achieve higher accuracy, besides a proper initialization, reducing the target height is an option. To achieve a lower millimeter-level accuracy, the pole can be reversed, and the AP20 AutoPole can be used in an upside-down configuration. The datasheet indicates an achievable accuracy of 1 mm $+0.1$ mm/° tilt for a target height of 0.228m in this configuration. However, this configuration was not considered in this study.

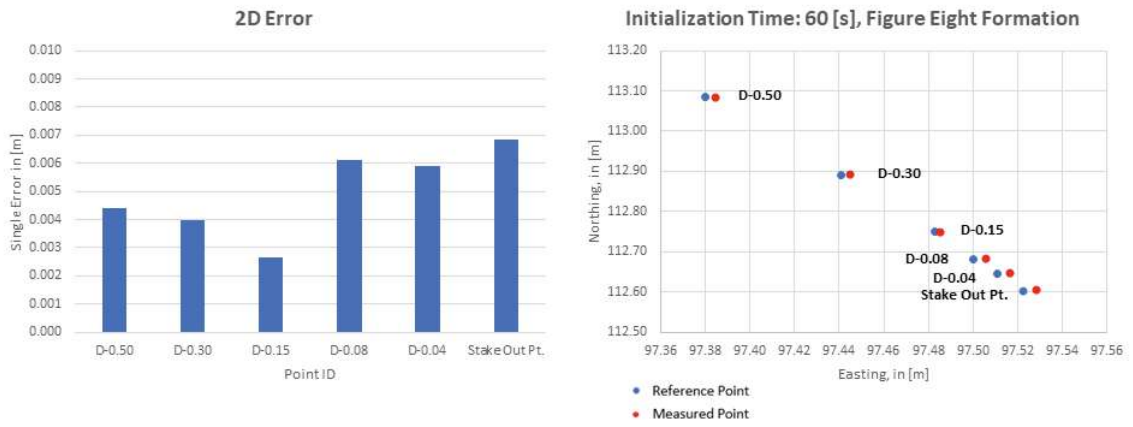

Figure 4.31: Stake out: 60[s] Initialization Time

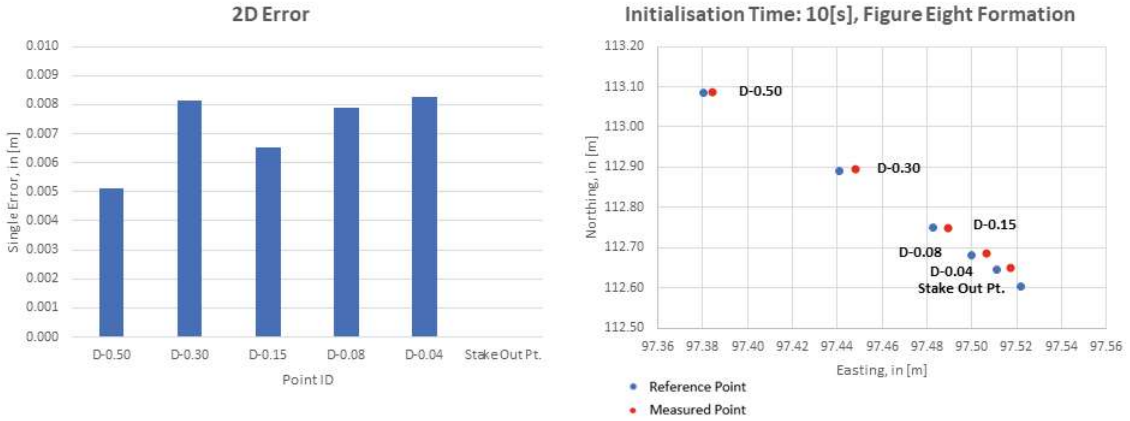

Figure 4.32: Stake out: 10[s] Initialization Time

If the initialization time is reduced to 10s, it can be observed that the deviation from the reference point is already quite high at the beginning (see fig. 4.32). Although it is evident that the deviation does not deteriorate significantly compared to the long initialization time in figure 4.31, in this experiment, the attitude quality threshold was exceeded, and the last point, the actual stakeout point, could not be measured. To continue, a re-initialization would need to be performed. However, since the stakeout point is already in close proximity, this re-initialization would only involve a minor additional effort for a user. But due to the comparability of the data with the other experiments in this section, this re-initialization was not carried out. It is therefore apparent that if an insufficiently accurate initialization is performed, it can lead to a disruption of the tilt compensation before the actual stakeout point is reached.
As shown in figure 4.31, a sufficient initialization phase circumvents this problem. However, it was also demonstrated that a lack of movement can lead to an increase in deviation even in this case. This raises the question of how this problem can be addressed.

As a solution, the following scenario was investigated: Before each short static phase, a figure eight formation was performed. This compensates for the lack of movement during navigation to the stakeout point. The horizontal accelerations also counteract the IMU drift in the phase and prevent the threshold from being exceeded.
It is evident that additional movement has a positive effect. Despite the long initialization phase, the error can be reduced to half, and with little movement between points (*D-0.08, D-0.04*, and the *Stake Out Pt.* itself), it can even be reduced to about one-third of the original deviation, which is shown in figure 4.33. Furthermore, a homogeneous distribution of the error in the range between 1mm to 3mm is observed, without any discontinuities. The positive effect is also pronounced with a shorter initialization time (see fig. 4.34).

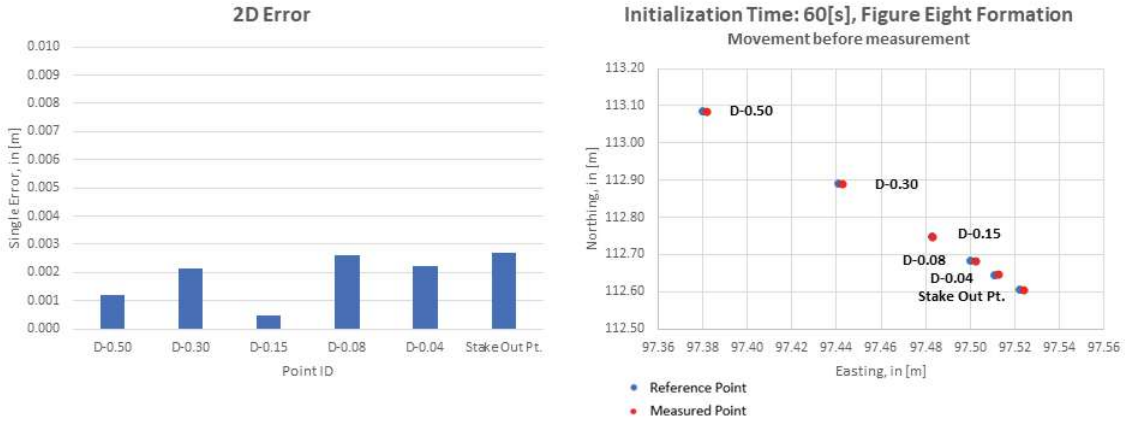

Figure 4.33: Stake out: 60[s] Initialization Time; short figure eight formation before each point

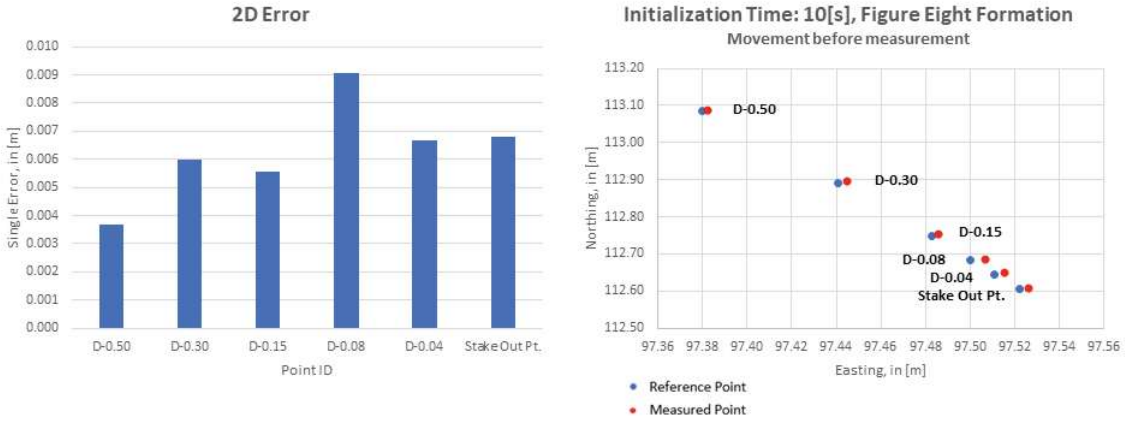

Figure 4.34: Stake out: 10[s] Initialization Time; short figure eight formation before each point

Although the level of error decreases less compared to the longer initialization time, it is evident that the initially higher level of error does not decrease here. If a short initialization time of 10 seconds is performed at the beginning along with additional brief movements along the path to the stake-out point, then, in contrast to the experiment shown in figure 4.32 without movements after the initialization phase, the stake-out point can be reached, and a comparable or even slightly lower 2D error at the stake-out point can be achieved.

From this, a best practice can be derived, which is also graphically represented in figure 4.35: a prolonged initialization phase with intermittent accelerations leads to a lower standard deviation of the attitude estimation. Consequently, this also translates into achievable accuracy. Additionally, in figure 4.35, a linear propagation of the further course of Q_{zz} is plotted. It is clear that the short movement phases lead to a decrease in the value of Q_{zz}. Therefore, additional movement phases, as the figure eight formation here, can be recommended even after a longer initialization phase.

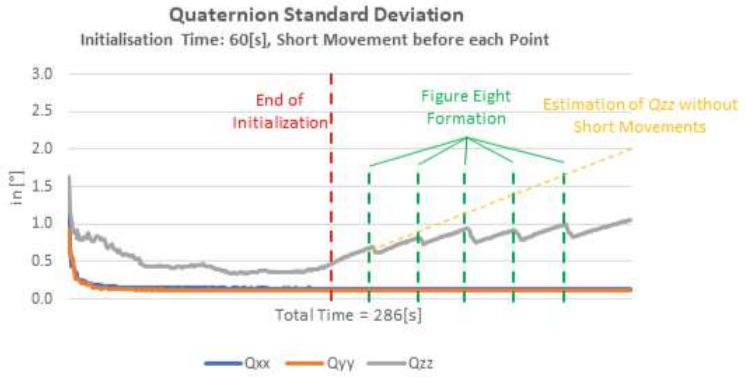

Figure 4.35: Effect of short movements even after a longer initialization phase

In summary, this experiment represents a somewhat simulated stake out situation. In common practice and through the experience of users, navigating to the point in a linear movement is more idealized in this experiment. Nevertheless, this experiment illustrates the fundamental problem of a deficient initialization phase in a practical environment well. It is evident that a longer initialization establishes a solid foundation, ensuring a relatively low level of deviation from the outset.

Furthermore, the results of this study demonstrate that with little movement of the AP20 AutoPole, for example, during navigation to the point, deviation can be reduced by movement with accelerations in the horizontal plane.

5. Summary and Outlook

Leica Geosystems has introduced an innovative product to the market with the AP20 AutoPole, which brings significant simplification to everyday surveying tasks. Among other features, the inclination compensation for terrestrial point acquisition using a total station is a real game-changer. Due to the lack of scientific literature at the time of this study, the goal was to focus specifically on practical aspects of the AP20 AutoPole through investigations.

The system was compared to conventional methods of point acquisition. It was found that point acquisition using the AP20 AutoPole corresponds to the accuracy level of a surveying pole stabilized using a bipod. A clear positive aspect is that, unlike conventional methods, the user receives immediate feedback on the actual, current accuracy of the point determination at the ground point. Previously, this was not the case, and the user only had an accuracy estimate of the measured point in the prism available during post-processing, not of the ground point. Despite the time lost for the initialization phase, a significant time saving can still be achieved overall as shown in fig. 4.6. A time saving of 25% was observed compared to conventional methods where the pole was stabilized with a bipod. This subsequently leads to a quick return on investment for the user.

In another experiment, a closer look was taken at the initialization phase. This is something new and unfamiliar for users, so this study identified best practices for initialization to enable more efficient use of the system. Starting with the duration of the initialization, it was found that an initialization phase of about 60s is ideal. Especially when little movement occurs afterwards, a longer initialization phase allows for a longer period during which the pole can be used with minimal movement. However, it was still shown that the handicap for phases with little movement is the drift of the yaw component, which is called "tilt direction" in the manufacturer's definition. To ensure a certain level of accuracy nonetheless, the manufacturer has defined a threshold above which the tilt compensation is stopped and only re-enabled after re-initialization.

The initialization phase serves to estimate inaccuracies of the IMU for processing in the Kalman filter. The better this estimation, the lower the drift of the IMU. The study presented different variants of initialization and evaluated them based on the attitude quality parameters provided by the manufacturer in the XML file of the measurement job in the field software. Methods that perform a variable movement in the horizontal plane were found to be particularly suitable as they lead to a rapid convergence of the quality parameters. Specifically, a figure eight formation in combination with an initialization time of 60s demonstrates particularly rapid convergence behavior and is therefore recommended based on the investigations conducted in this study (see fig. 5.1).

It was observed that the saturation level is crucial for the time until the threshold is

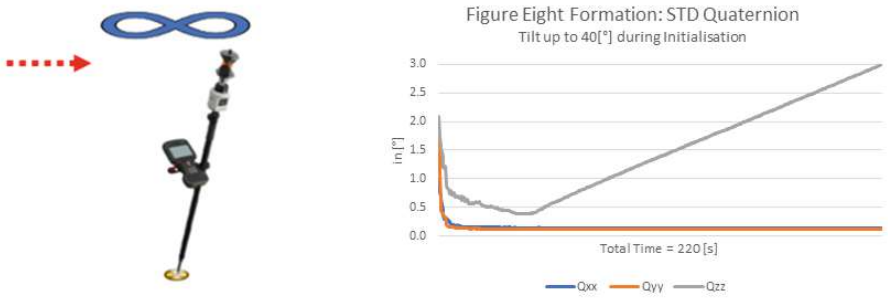

Figure 5.1: Based on the investigations, an initialization time of 60s in combination with a figure eight formation can be recommended for a good initialization result.

reached or exceeded. The lower this level, the longer the time until reaching or exceeding the threshold. To reduce this drift, a more accurate IMU would need to be installed by the manufacturer. However, it should be noted that long static phases are hardly a use case in everyday surveying. Finally, it was also observed that even after exceeding the threshold, a rapid convergence and thus a faster reaching of the saturation level occurs during re-initialization compared to the initial initialization. Based on these results, it can be concluded that a better IMU would have a positive effect on the drift phase, but simple measures by the user can counteract this drift, i.e. short pole movements after a (quasi-)static period.

In a subsequent examination, the findings regarding initialization were investigated in practical application. An everyday task in surveying was simulated. In a stakeout scenario, it was examined how the AP20 AutoPole behaves after initialization when navigating to a stakeout point. As the distance to this point decreases, the movement also decreases and becomes nearly static. It was found that with insufficient initialization time, the threshold would be exceeded before reaching the stakeout point, requiring re-initialization. With sufficient initialization time, it was demonstrated that the error to the actual point increases as movement decreases. To address this in reality, additional variable movement in the horizontal plane was incorporated in another attempt. This led to a noticeable improvement in results and a reduction in error.

For future investigations, questions remain about the extent to which the total station influences the initialization results and how this can be optimized. Similarly, the impact of a more accurate IMU on the overall system is also an important question to address. Similarly, the AP20 AutoPole could be further investigated in a kinematic environment. With robotics becoming increasingly prevalent in the construction sector, there is significant potential for the use of the AP20 AutoPole device as a sensor. Its robustness, water-

proofing, and compact design make it suitable for use in challenging external conditions. Additionally, data communication is already available.

In the future, tilt-compensated point measurement could become the state of the art in point determination using total stations like it is already in RTK GNSS sensors nowadays. With the AP20 AutoPole, the first product in this niche has been established in the market. Future products of this kind have the potential to become even easier to use and smaller in size. Moreover, products like the AP20 AutoPole could serve as a platform for further subsystems, bringing additional innovative technology and methods into future surveying. However, before this can happen, tilt-compensated measurements need to be established in the market.

In conclusion, the AP20 AutoPole provides support for users, both in terms of efficiency and by offering new possibilities. This includes direct feedback on the current quality of point determination at the pole tip, as well as an expansion of the application of point measurements using a pole. Nevertheless, the overall system also requires users to engage with new aspects. This work addresses these new points to contribute to an improved experience in the application of the AP20 AutoPole.

References

- Bayoud, F. (2006): *Leica's Pinpoint EDM Technology with Modified Signal Processing and Novel Optomechanical Features*, In: Proceedings vom XXIII FIG Congress, Munich, Germany, 2006
- Bluetooth SIG (2024): *Bluetooth Low Energy Primer*, https://www.bluetooth.com/wp-content/uploads/2022/05/the-bluetooth-le-primer-v1.2.0.pdf, Version 1.2.0., Bluetooth SIG: Kirkland (WA), USA, 2024
- Groves, P. D. (2013): *Principles of GNSS, Inertial, and Multisensor Integrated Navigation Systems*, Second Edition, Artech House: Norwood, MA, USA, 2013.
- Joeckel, R.; Stober, M.; Huep, W. (2008): *Elektronische Entfernungs- und Richtungsmessung und ihre Integration in aktuelle Positionierungsverfahren*, 5. Auflage, Wichmann Verlag: Heidelberg, Germany, 2008
- Kleemaier, G. (2018): *Multisensorsystem Totalstation*, In: DVW e.V. (Hrsg.): MST 2018 – Multisensortechnologie: Low-Cost Sensoren im Verbund. DVW Schriftenreihe, Band 92, p. 25-36, Augsburg, Germany, 2018
- Lackner, S.; Lienhart, W. (2016): *Impact of Prism Type and Prism Orientation on the Accuracy of Automated Total Station Measurements*, In: Proc. Joint International Symposium on Deformation Monitoring (JISDM). pp. 8p, Joint International Symposium on Deformation Monitoring (JISDM), TU Wien, Austria, 2016
- Leica Geosystems (2022): *Leica TS60/MS60/TM60 User Manual (en)*, Version 5.0.0, Leica Geosystems AG: Heerbrugg, Switzerland, 2022
- Leica Geosystems (2022): *Leica AP20 AutoPole Data Sheet*, Leica Geosystems AG: Heerbrugg, Switzerland, 2022
- Leica Geosystems (2023): *Leica Captivate Technical Reference Manual (en)*, Version 8.0, Leica Geosystems AG: Heerbrugg, Switzerland, 2023
- Luo, X.; Schaufler, S.; Carrera, M.; Celebi, I. (2018): *High-Precision RTK Positioning with Calibration-Free Tilt Compensation*, In: Proceedings of FIG Congress 2018, Instanbul, Turkey, 2018
- Maar, H. (2022): *Leica AP20 White Paper*, Leica Geosystems AG: Heerbrugg, Switzerland, 2022

- Maar, H.; Zogg, H. M. (2017): *Leica Nova MS60 White Paper*, Leica Geosystems AG: Heerbrugg, Switzerland, 2017
- Teodori, G. (2019): *Simulationsstudien zur Verbesserung der Gierwinkelschätzung bei der losen INS-GNSS-Kopplung*, Master Thesis, Vienna University of Technology: Austria, 2019
- Thalmann, T.; Zechner, M.; Neuner, H.-B. (2020): *Accelerometer Triad Calibration for Pole Tilt Compensation Using Variance Based Sensitivity Analysis*, Sensors 2020, 20, 1481. https://doi.org/10.3390/s20051481, Basel, Switzerland, 2020
- Titterton, D.; Weston, J. L. (2004): *Strapdown Inertial Navigation Technology*, 2nd ed., IET: London, United Kingdom, 2004
- Zogg, H.-M.; Lienhart, W.; Nindl, D. (2009): *Leica TS30 White Paper*, Leica Geosystems AG: Herrbrugg, Switzerland, 2009

List of Figures

A. Case Study : Comparison of Pole Measurement (section 4.1)

Representation of the 2D single errors, divided into Easting and Northing components

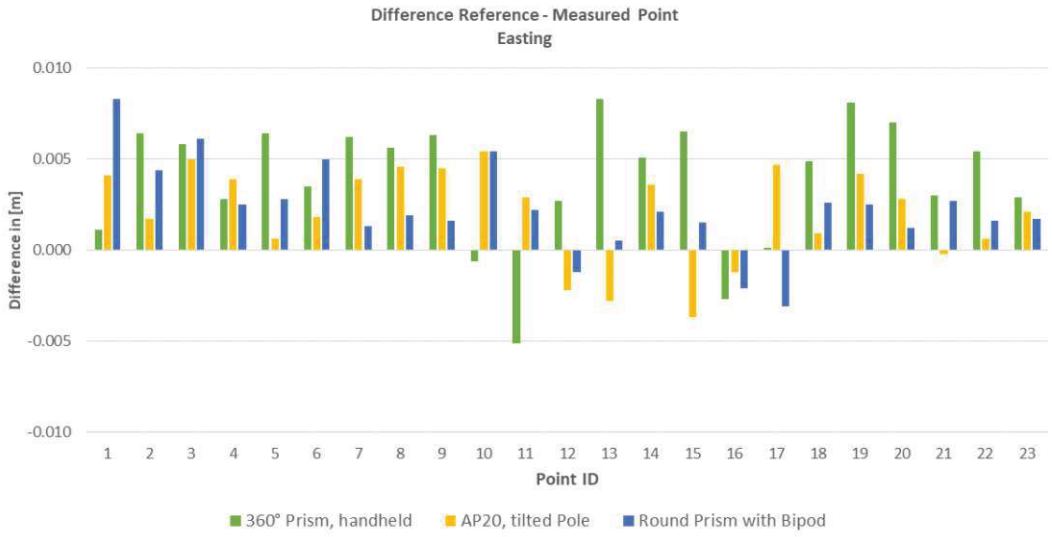

Figure A.1: Deviation from the reference point, separated in Easting and Northing component

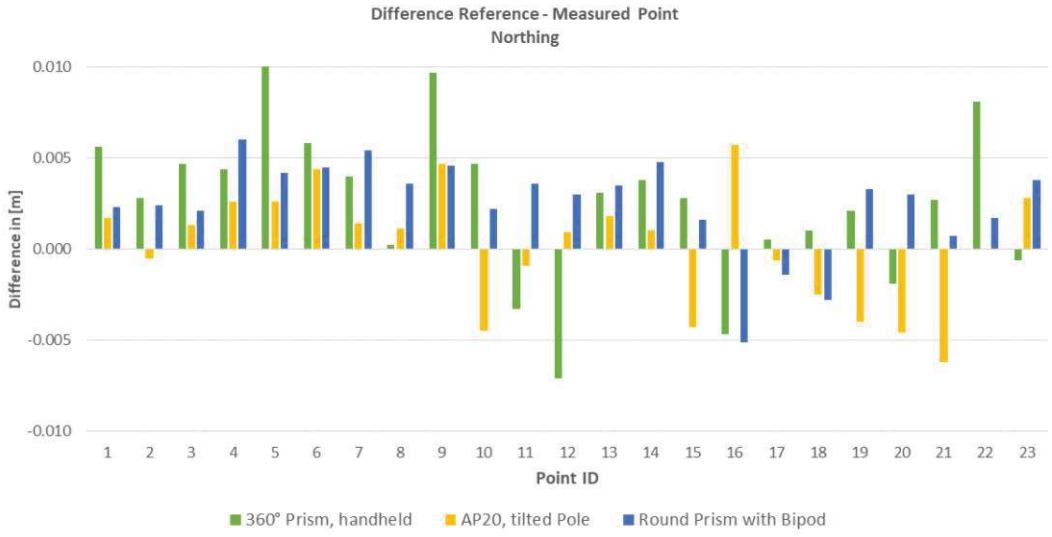

Figure A.2: Deviation from the reference point, separated in Easting and Northing component

Histograms showing the probability of 2D and 1D single error

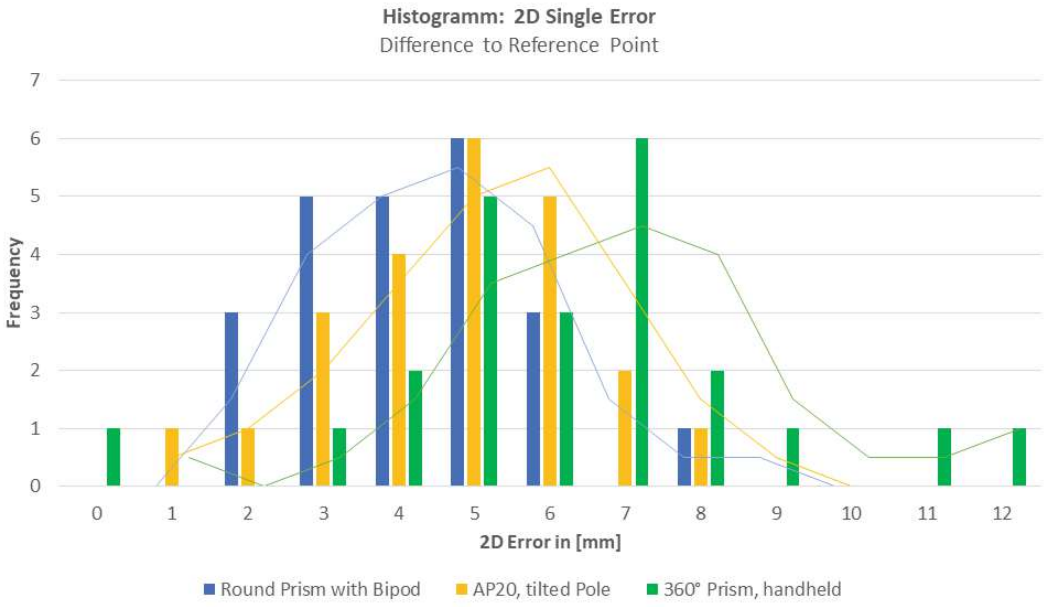

Figure A.3: Probability of 2D single error values

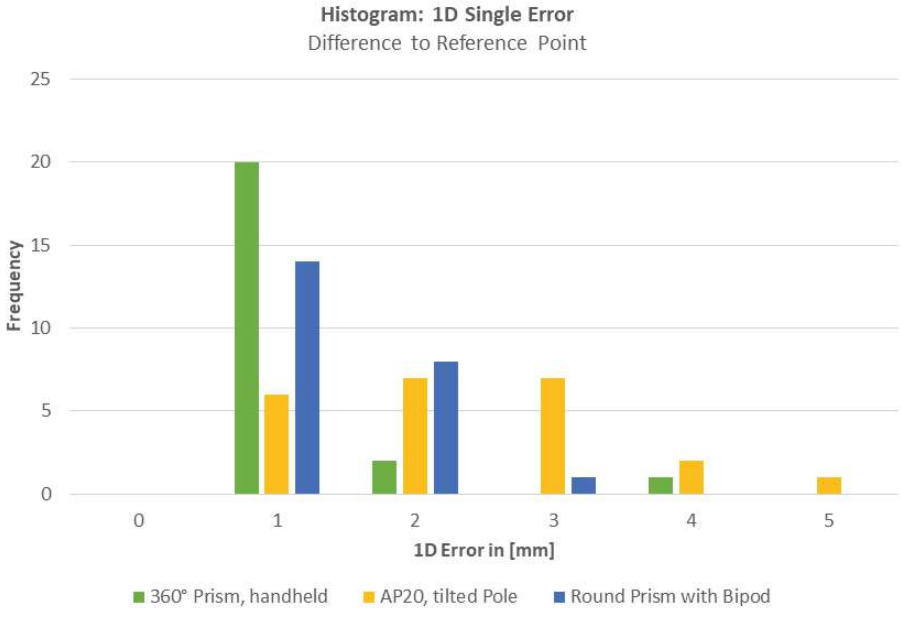

Figure A.4: Probability of 1D single error values

B. Analysis on Initialization and Influence on Tilt-Compensated Measurements (section 4.2)

Figures of Initialization Periods 3s and 10s:
Roll-Pitch-Yaw during static phase

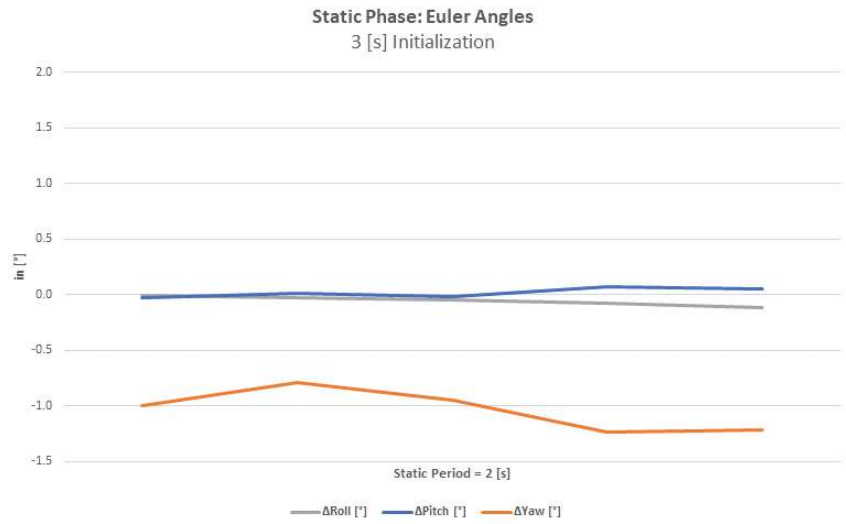

Figure B.1: 3s Initialization: Timespan after initialization phase until tilt compensation is stopped. The pole is stabilized.

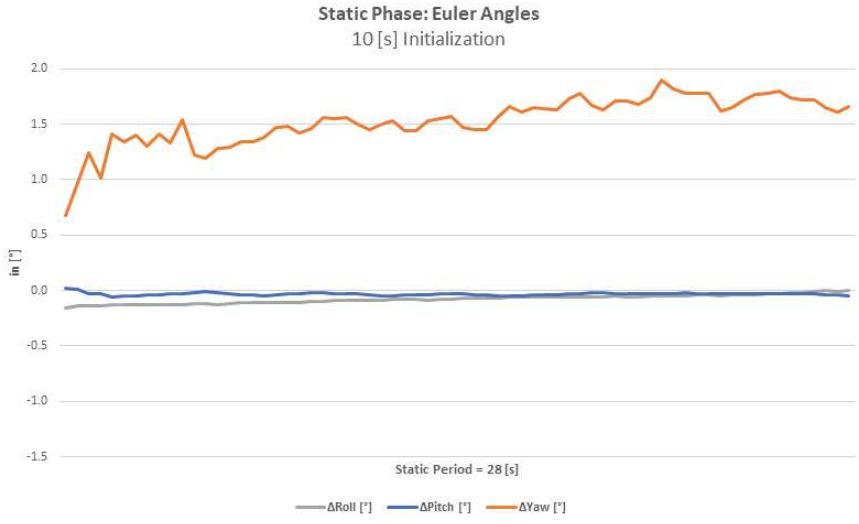

Figure B.2: 10s Initialization: Timespan after initialization phase until tilt compensation is stopped. The pole is stabilized.

Easting-Northing-Height during static phase

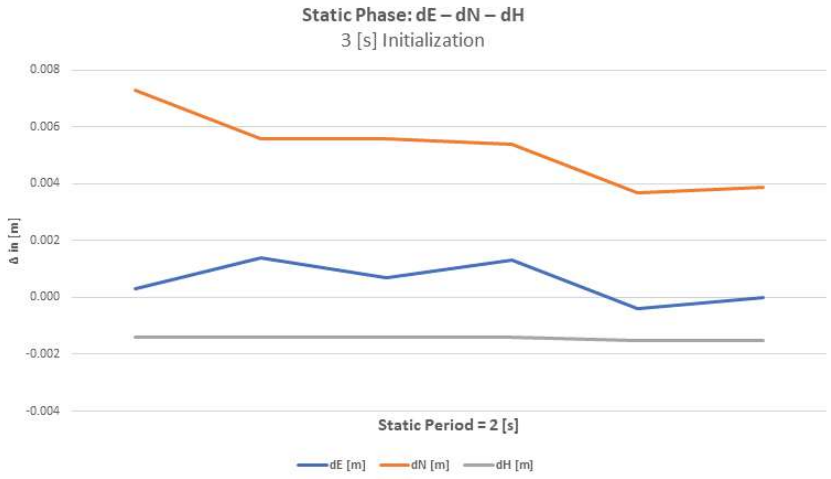

Figure B.3: 3s Initialisation: Drift of ENH coordinates over time during static phase with reference to the first point of static phase

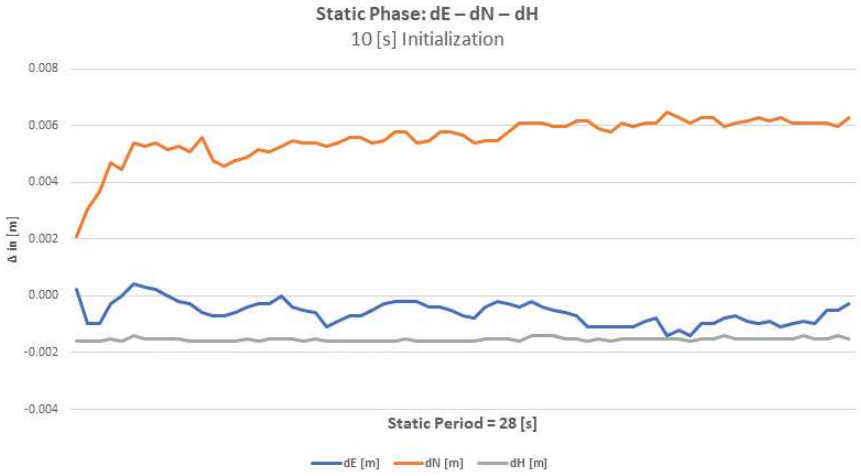

Figure B.4: 10s Initialisation: Drift of ENH coordinates over time during static phase with reference to the first point of static phase